An efficient hybrid method for solving Euler equations

U S Vevek, Zang B.[+] and New T. H.*

School of Mechanical and Aerospace Engineering, Nanyang Technological University

50 Nanyang Avenue, Singapore 639798

+ Currently at Department of Aerospace Engineering, University of Bristol

Bristol BS8 1TR, United Kingdom

Abstract

In this paper, a hybrid method suitable for solving the Euler equations using high order methods has been proposed. The method was implemented and validated with a seventh-order WENO scheme in OpenFOAM®. The hybrid method combines a simple MUSCL-type flux approach and a characteristic flux approach. In the MUSCL-type flux approach, the inviscid fluxes are computed using approximate Riemann solvers HLL and HLLC schemes based on the WENO-reconstructed state variables. Hence, this is dubbed as the VF (variable-based flux) approach. In critical regions where VF may produce spurious oscillations, a novel, low-dissipation HLL-based CF (characteristic flux) approach is applied. Critical regions were identified using a modified Bhagatwala-Lele shock sensor. The VF/CF hybrid method has been shown to produce high-resolution, essentially non-oscillatory results for a number of 1D and 2D problems at a fraction of the cost of a pure CF approach. Moreover, a 2D advection problem was designed to investigate the choice of state variables and flux schemes. The results have shed more light on the relation between Kelvin-Helmholtz roll-ups and numerical instabilities along slip lines.

Keywords: Euler equations; hybrid method; high order WENO schemes; characteristic fluxes; shock sensor.

*Corresponding author: dthnew@ntu.edu.sg

1 Introduction

Compressible flow problems are challenging to simulate due to the presence of discontinuities such as shock waves and contact discontinuities. Shock capturing strategies are able to capture the discontinuities by introducing sufficient numerical dissipation to suppress the formation of spurious Gibbs-like oscillations. However, such dissipation is detrimental in smooth regions of the solutions. For instance, the TVD (total-variation-diminishing) scheme introduced by Harten [1], which captures discontinuities in a non-oscillatory manner by reverting to being only first order accurate near steep gradients, is known to 'clip' even smooth extrema. High order accuracy is required in smooth parts of the solution to be able to resolve the smaller length scales [2]. It is well known that high order numerical schemes can capture vortical interactions in the flow more accurately with a significantly smaller number of mesh cells than their low order counterparts [3]. Hence, they are particularly suitable in large-scale simulations, such as simulations of a high-speed compressible jet (which requires an extended domain for full development) and of flow past a lifting surface (which requires an appropriate spanwise length to better capture the 3D effects).

Progress was made in the design of high order shock capturing techniques with the development of ENO (essentially non-oscillatory) schemes [4] which overcame the drawback of TVD schemes by maintaining a high order accuracy and low dissipation in smooth regions. ENO schemes involve the selection of an optimal stencil for high order spatial reconstruction. The ENO scheme was made more robust by Liu, et al. [5] who proposed to take an average of the reconstructions from all candidate stencils weighted based on the local smoothness of the solution with the stencil. This *weighted* ENO (WENO) scheme allowed the overall scheme to achieve an even higher order of accuracy compared to the individual stencils. Later, Jiang and Shu [6] improved upon the WENO scheme with a modified smoothness indicator which allowed the scheme to achieve optimal accuracy. After nearly a decade, it was discovered that the WENO scheme does not converge at the optimal order of accuracy near critical points [7]. Therefore, several variations have been proposed since then to rectify this problem [7-13]. In this study, however, a seventh order WENO scheme based on Jiang and Shu's formulation was used,

as the variations of WENO scheme can be readily adopted with the proposed hybrid approach in the present study.

Apart from a suitable spatial reconstruction scheme, computing the inviscid fluxes of the Euler equations also requires an upwind numerical flux scheme. These numerical flux schemes are based on Godunov's approach [14] of solving the Riemann problem at cell interfaces. Godunov represented the solution within each cell to be uniform, which is effectively the first-order accurate upwind spatial reconstruction scheme. van Leer [15] extended the approach to second order by representing the solution within each cell to be linearly varying in his famous MUSCL approach. Since an exact Riemann solver is costly and time-consuming, approximate Riemann solvers are utilized in almost all practical algorithms. For an excellent introduction on Riemann solvers, refer to Ref. [16]. The MUSCL approach with approximate Riemann solvers is computationally cheap and robust. However, it does not guarantee oscillation-free results when the solution within each cell is reconstructed using high order methods. Qiu and Shu [17] showed that component-wise reconstructions using high order WENO schemes lead to the formation of spurious oscillations which can be remedied by performing the WENO reconstruction in characteristic space. However, this requires the costly process of projecting the solution into the characteristic space using a local characteristic decomposition. Therefore, for large scale simulations, it is not practical to apply characteristic fluxes. Instead, a hybrid method would be a more prudent and efficient choice.

The concept of a hybrid method simply involves overcoming the weaknesses of one method with the strength of another. Adams and Shariff [18] proposed a hybrid of non-conservative compact scheme and a conservative ENO scheme which switches from the former in smooth regions to the latter near discontinuities. Pirozzoli [19] modified it by coupling a conservative compact scheme with a WENO scheme. The success of a hybrid method in terms of accuracy and efficiency depends on the mechanism used to switch from one method to the other. Both these hybrid methods used simple switching mechanisms based on the absolute difference between the solutions in adjacent grid points. Since this mechanism caused abrupt switching between the schemes and produce spurious waves, Ren, et al. [20] introduced a weighted characteristic-wise hybrid method coupling the compact scheme and WENO

scheme using a continuous weight function based on the absolute difference between the solutions in adjacent grid points. Kim and Kwon [21] proposed a slightly different hybrid method that was a weighted average of a central scheme and a WENO scheme. They also investigated several possible weighting functions. Their hybrid central-WENO scheme achieved equally good resolution as the characteristic-wise hybrid compact-WENO scheme of Ren, et al. but it was reported to take only half the time with certain weighting functions. Costa and Don [22] used a multiresolution procedure to identify the critical regions where WENO should be used. They reported that the hybrid scheme was considerably faster than a pure WENO scheme and that the speedup increased with the size of the problem. More recently, Hu, et al. [23] proposed a hybrid of a 'component-wise' flux reconstructed using an optimal linear scheme and a characteristic-wise flux reconstructed using WENO scheme. Their 'component-wise' flux computation still involved a local characteristic decomposition and projection but related in a lower floating-point operation count than a fully characteristic-wise flux computation. Yet another hybrid method was recently proposed by Peng, et al. [24] who coupled a component-wise flux and a characteristic-wise flux both reconstructed using WENO scheme. A novel aspect of their work is the use of a discontinuity detector based on the WENO weights only. Lee, et al. [25] implemented a hybrid scheme in OpenFOAM® coupling a central non-dissipative flux and a central-upwind dissipative flux weighted by the Bhagatwala-Lele shock sensor [26], a variant of the Ducros sensor [27] which uses the flow dilatation to determine compressive regions. This sensor is able to distinguish between steep compressive gradients and turbulent fluctuations much better than simple difference-based sensors. Unlike the previous methods, their hybrid method uses low order TVD scheme for computing the dissipative flux near shocks rather than high order characteristic fluxes.

Inspired by its computational efficiency, a WENO-based hybrid method is proposed in the present paper as a possible candidate for high order large-scale simulations. The design of the hybrid solver bears some resemblance to that proposed by Peng, et al. [24] since both sub-schemes employ WENO reconstructions but there are important differences between the two. Firstly, encouraged by the results from Lee, et al. [25], the critical regions are identified by a modified Bhagatwala-Lele shock sensor. Secondly, in non-critical regions, WENO schemes are used to reconstruct state *variables* in the present

hybrid solver rather than the split fluxes as done conventionally for high order WENO schemes. The reconstructed state variables are then used to compute the numerical flux using HLL and HLLC approximate Riemann solvers in a MUSCL-type approach. Both primitive and conservative variables are reconstructed in this study. Thirdly, a novel characteristic flux scheme based on HLL flux is applied in the critical region which is shown to be less dissipative than the Lax-Friedrich or Rusanov approaches [6]. Subsequently, the paper is arranged as follows: the seventh order WENO scheme will be briefly introduced in Section 2. The hybrid method will be detailed in Section 3. The performance of the hybrid scheme will be illustrated using a number of 1D and 2D test cases in Section 4 including discussions on various aspects of the hybrid scheme. Finally, the conclusions will be given in Section 5.

2 Numerical methods

The equations governing the dynamics of inviscid gas flow are given below. They are collectively referred to as the Euler equations. ρ, $\boldsymbol{u}$, p and E refer to the gas density, velocity, pressure and specific total energy, respectively.

$$\partial_t \begin{pmatrix} \rho \\ \rho\boldsymbol{u} \\ \rho E \end{pmatrix} + \nabla \cdot \begin{pmatrix} \rho\boldsymbol{u} \\ \rho\boldsymbol{u}\boldsymbol{u} + p\mathrm{I} \\ \rho E\boldsymbol{u} + p\boldsymbol{u} \end{pmatrix} = \begin{pmatrix} 0 \\ \mathbf{0} \\ 0 \end{pmatrix} \quad \text{where } E = \frac{p}{(\gamma-1)\rho} + \frac{\boldsymbol{u}\cdot\boldsymbol{u}}{2} \tag{1}$$

As shown in Eq. (1), the total energy comprises of the internal and kinetic energies and the expression for internal energy is obtained from the ideal gas law. γ refers to the ratio of specific heat capacities which is taken to 1.4 in the present study. The procedure to solve these equations will be discussed in detail in the following sections.

2.1 Finite volume methodology

The finite volume methodology (FVM) is employed in solving the Euler equations. In FVM, the domain is discretized into non-overlapping cells and the solution is obtained in terms of the cell averages. Given a function $\phi(\boldsymbol{x})$, its cell average over the i^{th} cell Ω_i is given by

$$\overline{\phi_i} \equiv \frac{1}{|\Omega_i|} \iiint_{\Omega_i} \phi(\boldsymbol{x})\, dV \tag{2}$$

where $|\Omega_i|$ refers to the volume of the cell.

The Euler equations can be represented in the general form shown below.

$$\partial_t \boldsymbol{W} + \nabla \cdot F(\boldsymbol{W}) = \boldsymbol{0} \tag{3}$$

Averaging Eq. (3) over Ω_i and applying the definition of cell average from Eq. (2), a system of ordinary differential equations (ODE) can be obtained for the evolution of the cell averages $\overline{\boldsymbol{W}_i}$. As is customary in FVM, the volume integral of the divergence term has been transformed into a surface integral over $\partial\Omega_i$, the boundary of Ω_i, through the use of Gauss theorem.

$$\frac{1}{|\Omega_i|} \iiint_{\Omega_i} \left[\partial_t \boldsymbol{W} + \nabla \cdot F(\boldsymbol{W}) \right] = \boldsymbol{0} \quad \Rightarrow \quad \frac{d\overline{\boldsymbol{W}_i}}{dt} = -\frac{1}{|\Omega_i|} \oiint_{\partial\Omega_i} F(\boldsymbol{W}) \cdot \boldsymbol{dS} \tag{4}$$

It must be remarked that the derivation thus far has been exact. The main approximation in FVM lies in the calculation of fluxes at the cell boundary $\partial\Omega_i$. The accuracy of the solution depends directly on the approximation of the surface integral in Eq. (4).

For a one-dimensional problem solved on a uniform grid such that $|\Omega_i| = \Delta x$, Eq. (4) simplifies to the following whereby the physical flux function F has been replaced by a *numerical* flux function $\widehat{F}$ to provide the necessary upwinding. The operator L on the RHS of Eq. (5) denotes the combined operation of the spatial reconstruction and numerical flux schemes.

$$\frac{d\overline{\boldsymbol{W}_i}}{dt} = -\frac{1}{\Delta x} \left[\widehat{F}_{i+1/2} - \widehat{F}_{i-1/2} \right] = L\left(\overline{\boldsymbol{W}_i}, \overline{\boldsymbol{W}_{i\pm1}}, \ldots \right) \tag{5}$$

$\widehat{F}_{i+1/2}$ and $\widehat{F}_{i-1/2}$ denote the numerical fluxes at the right and left cell boundaries of the i^{th} cell, respectively. The evaluation of $\widehat{F}_{i\pm1/2}$ requires approximation of the fluxes at the cell boundaries based on the cell averages $\overline{\boldsymbol{W}_i}$ using spatial reconstruction schemes (i.e. WENO schemes in the present study).

2.1.1 Time marching

Given the solution $\overline{\boldsymbol{W}_i^n}$ at time step n, the ODE in Eq. (5) can be marched in time to the next time step $n+1$ using the third order TVD Runge-Kutta method [28] given below.

$$\begin{aligned}
\overline{\boldsymbol{W}_i^{(1)}} &= \overline{\boldsymbol{W}_i^n} + \Delta t \cdot L\left(\overline{\boldsymbol{W}_i^n}, \overline{\boldsymbol{W}_{i\pm1}^n}, \ldots\right) \\
\overline{\boldsymbol{W}_i^{(2)}} &= \frac{3}{4}\overline{\boldsymbol{W}_i^n} + \frac{1}{4}\left[\overline{\boldsymbol{W}_i^{(1)}} + \Delta t \cdot L\left(\overline{\boldsymbol{W}_i^{(1)}}, \overline{\boldsymbol{W}_{i\pm1}^{(1)}}, \ldots\right)\right] \\
\overline{\boldsymbol{W}_i^{n+1}} &= \frac{1}{3}\overline{\boldsymbol{W}_i^n} + \frac{2}{3}\left[\overline{\boldsymbol{W}_i^{(2)}} + \Delta t \cdot L\left(\overline{\boldsymbol{W}_i^{(2)}}, \overline{\boldsymbol{W}_{i\pm1}^{(2)}}, \ldots\right)\right]
\end{aligned} \tag{6}$$

2.1.2 Extension to higher dimensions

For two- or three-dimensional problems, one could perform a truly multi-dimensional spatial reconstruction of the solution followed by a multi-point quadrature to evaluate the surface integral in Eq. (4) [29, 30]. However, such an approach can be difficult to implement and, more importantly, computationally demanding and expensive. Thus, in order to strike a balance between numerical accuracy and computational efficiency/robustness, the present WENO scheme is implemented with the dimension-by-dimension approach (also known as dimensional split approach) [6] whereby spatial reconstruction is performed only along the face normal direction and the fluxes are evaluated only at the face centers. This approach is illustrated in Figure 1 for a two-dimensional uniform Cartesian grid. The cells shaded grey form the *stencil* used for seventh order WENO reconstruction at the respective faces outlined in red. The stencil for each face (a list of cell indices) is built in a recursive manner by searching the mesh along the unit face normal direction $\boldsymbol{n}_f$.

With this simplification, Eq. (5) can be generalized for higher dimensions as,

$$\frac{d\overline{\boldsymbol{W}_i}}{dt} \approx -\frac{1}{|\Omega_i|}\sum_f \widehat{F}_f \cdot \boldsymbol{S}_f \quad \text{where } \boldsymbol{S}_f \equiv \boldsymbol{n}_f S_f \tag{7}$$

where S_f is the surface area of face f. Upon the evaluation of the numerical fluxes $\widehat{F}_f$ at all the faces, the right-hand side of Eq. (7) can be computed easily using existing tools in OpenFOAM.

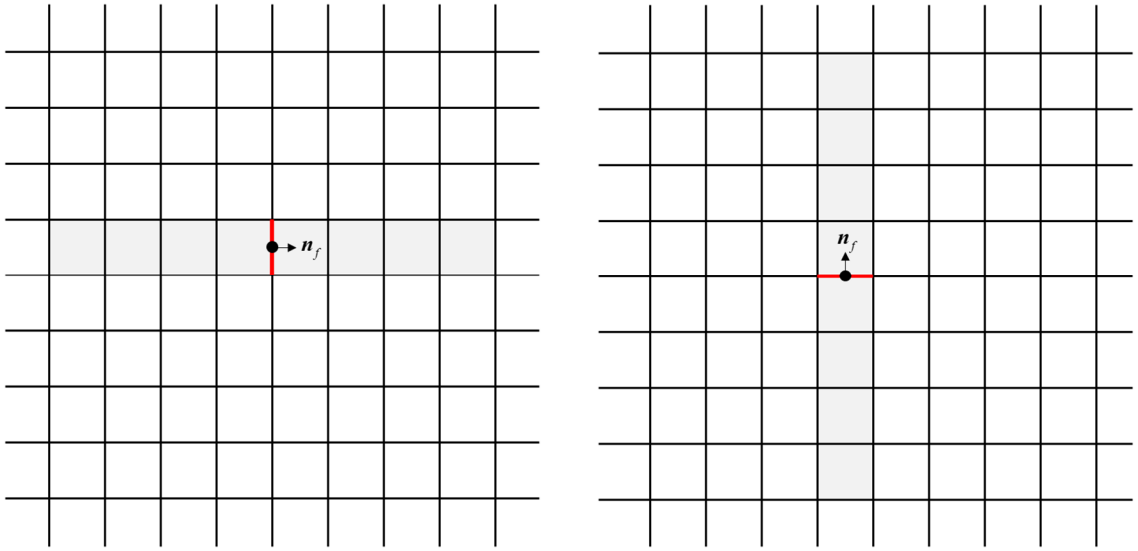

Figure 1: Numerical flux at cell interface (outlined red) is evaluated at face center (black circle) using cells only along face-normal direction (shaded grey). $\boldsymbol{n}_f$ (black arrow) denotes face unit normal vector.

It must be remarked that this approach is formally only second order accurate, but this does *not* entail that it is no better than using second order schemes. For a given mesh, the use of high order spatial reconstruction has been observed to reduce the numerical dissipation of the scheme and improve its resolving capability. For instance, Ritos, et al. [31] compared second order MUSCL scheme and ninth order WENO scheme implemented using the dimensional split approach for performing implicit large-eddy simulations (ILES). Only the ninth order WENO scheme delivered results that matched with results obtained from experiments and/or direct numerical simulations (DNS). Furthermore, in a related study, they concluded that using high order schemes on coarser meshes is computationally more efficient than using low order schemes on finer meshes [32].

2.2 WENO scheme

Evaluation of the numerical flux at each face requires the left-biased and right-biased spatial reconstruction of the solution variables. The left and right sides are locally defined with respect to the face normal vector $\boldsymbol{n}_f$. In OpenFOAM, each internal face straddles two cells which are referred to as its owner (index P) and neighbor (index N) such that P < N. The vector $\boldsymbol{n}_f$ is uniquely defined to point

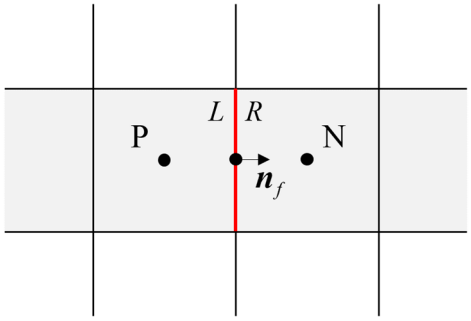

Figure 2: Definition of left (L) and right (R) sides for a given face (outlined red) with respect to the face normal vector $\boldsymbol{n}_f$ and the owner (P) and neighbour (N) cells.

from the owner into the neighbour. For a given face, the left side (L) is taken to be the owner side and the right side (R) is taken to be the neighbour side as shown in Figure 2.

Since the variable to be reconstructed may vary in a non-smooth manner, by Godunov's theorem [14] a linear reconstruction scheme higher than first order would introduce spurious oscillations which may render the algorithm unstable. Hence, a non-linear reconstruction scheme, which is mindful of the local behavior of the variable to be reconstructed, is required. WENO schemes are one such class of non-linear schemes. In this study, a seventh order WENO scheme was used and its spatial reconstruction procedure will be described next.

The stencil for seventh order WENO reconstruction at cell interface $i+\frac{1}{2}$ spans across eight cells from $i-3$ to $i+4$. The stencil is divided into five sub-stencils (j=0,1,2,3,4) each consisting of four cells. Sub-stencils j=0 to j=3 are used for the left-biased reconstruction while sub-stencils j=1 to j=4 are used for the right-biased reconstruction. The reconstruction direction x is the non-dimensional distance from the face centre $\boldsymbol{x}_f$ along the local face normal direction $\boldsymbol{n}_f$, i.e.

$$x = \frac{\boldsymbol{x} - \boldsymbol{x}_f}{\left\| \boldsymbol{x}_\mathrm{P} - \boldsymbol{x}_\mathrm{N} \right\|} \cdot \boldsymbol{n}_f \tag{8}$$

Consider the spatial reconstruction of the density variable $\rho(x)$. Each sub-stencil j results in a third order polynomial,

$$\rho_j(x) = \left(\rho_{i+1/2}\right)_j + \sum_{k=1}^{3} a_{k,j} x^k \tag{9}$$

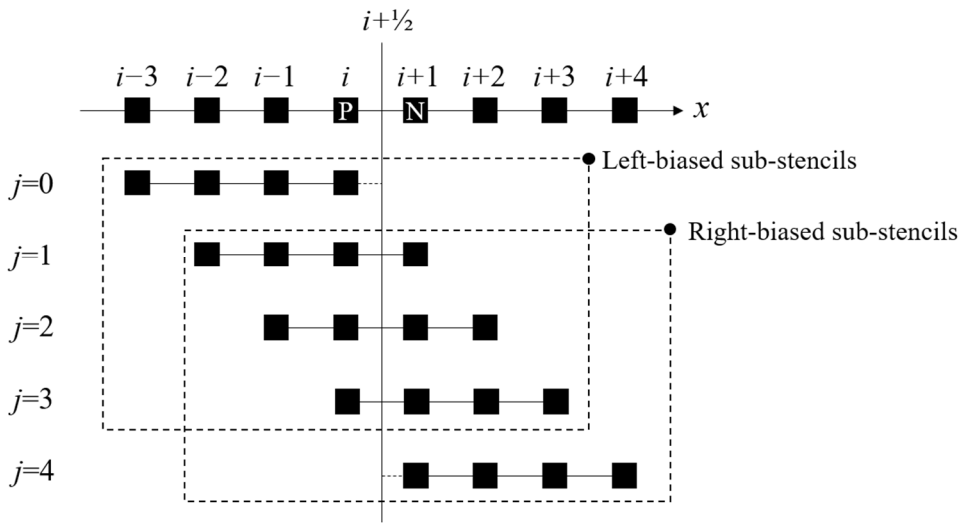

Figure 3: Stencil and sub-stencils for seventh order WENO reconstruction.

where $\left(\rho_{i+1/2}\right)_j$ is the fourth order approximation of the density at the cell interface and $a_{k,j}$ are the polynomial coefficients. These four quantities can be evaluated from the cell averages of the j^{th} sub-stencil. Readers are advised to refer to Appendix A for the details of the polynomial coefficients with respect to the seventh order WENO scheme.

The fourth order approximations from the sub-stencils from the respective sides can be combined using a weighted average to obtain seventh order *u*pstream *c*entral approximations $\left(\rho_{i+1/2}^{UC7}\right)_K$ using the ideal stencil weights $d_{j,K}$ as shown in Eq. (10). Note that subscript *K* is used to denote the sides *L* and *R*.

$$\begin{aligned}
\left(\rho_{i+1/2}^{UC7}\right)_L &= \sum_{j=0}^{3} d_{j,L}\left(\rho_{i+1/2}\right)_j \quad \text{where} \quad d_{j,L} = \left\{\frac{1}{35}, \frac{12}{35}, \frac{18}{35}, \frac{4}{35}\right\} \\
\left(\rho_{i+1/2}^{UC7}\right)_R &= \sum_{j=0}^{3} d_{j,R}\left(\rho_{i+1/2}\right)_{j+1} \quad \text{where} \quad d_{j,R} = \left\{\frac{4}{35}, \frac{18}{35}, \frac{12}{35}, \frac{1}{35}\right\}
\end{aligned} \tag{10}$$

Being a linear scheme, the upstream central approximation would introduce spurious oscillations. To ensure the essentially non-oscillatory property, the WENO approximation $\left(\rho_{i+1/2}^{W7}\right)_K$ is obtained by using non-linear sub-stencil weights $\omega_{j,K}$ instead of the ideal weights $d_{j,K}$.

$$\left(\rho_{i+1/2}^{W7}\right)_L = \sum_{j=0}^{3} \omega_{j,L} \left(\rho_{i+1/2}\right)_j$$
$$\left(\rho_{i+1/2}^{W7}\right)_R = \sum_{j=0}^{3} \omega_{j,R} \left(\rho_{i+1/2}\right)_{j+1} \tag{11}$$

The non-linear weights $\omega_{j,K}$ are computed as

$$\alpha_{j,K} = \frac{d_{j,K}}{\left(IS_{j,K} + \epsilon\right)^2}, \qquad \omega_{j,K} = \frac{\alpha_{j,K}}{\sum_{j=0}^{3} \alpha_{j,K}} \tag{12}$$

where $\epsilon = 10^{-6}$ is small number to prevent division by zero and $IS_{j,K}$ is the smoothness indicator of the polynomial $\rho_j(x)$. In this study, the smoothness indicator proposed by Jiang and Shu [6] was used. They can be expressed in a general positive semi-definite form in terms of the polynomial coefficients as shown below. Readers are advised to refer to Appendix B for the derivation of smoothness indicators.

$$IS_{j,K} = \left(a_{1,j} + r a_{2,j} + a_{3,j}\right)^2 + \frac{13}{3}\left(a_{2,j} + r\frac{3}{2}a_{3,j}\right)^2 + \frac{781}{20}a_{3,j}^2 \quad \text{where} \quad r = \begin{cases} -1, & \text{if } K = L \\ +1, & \text{if } K = R \end{cases} \tag{13}$$

The advantage of using this form to compute $IS_{j,K}$ will be become apparent later.

3 Hybrid method

3.1 Variable-based fluxes (VF)

One could simply evaluate the numerical flux at a face based on the left- and right-biased WENO interpolations of a set of state variables $\boldsymbol{V}$ at that face in a MUSCL-type fashion. This will be referred to as variable-based flux (VF) approach in this paper. Evaluating the numerical fluxes based on the reconstructed variables is computationally more efficient than reconstructing the fluxes in a component-wise fashion for two key reasons. Firstly, state variables are usually readily available while the left- and right-going fluxes have to computed from the state variables prior to reconstruction. Secondly, when reconstructing fluxes, the left- and right-going fluxes have to be reconstructed using the right- and left-

biased sub-stencils (see Figure 3), respectively. Essentially, these fluxes are two *different* quantities whose reconstruction involve eight third order polynomial reconstructions. On the other hand, when reconstructing variables, the *same* quantity is being reconstructed from both directions which involve only five third order polynomial reconstructions. The third order polynomial coefficients $a_{k,j}$ need to be computed only once for each sub-stencil j. This is the main advantage of computing $IS_{j,K}$ in terms of the polynomial coefficients as shown in Eq. (13). This advantage can be exploited to optimize the WENO reconstruction procedure for state variables to incur fewer floating-point operations compared to the traditional implementation.

There are several possibilities for the choice of reconstruction variables $\boldsymbol{V}$. In this study, both the primitive variables $\boldsymbol{V}=\left[\rho, \boldsymbol{u}, p\right]$ and the conservative variables $\boldsymbol{W}=\left[\rho, \rho\boldsymbol{u}, \rho E\right]$ were used and the effect of the choice of variables will be discussed in a later section.

One of the simplest yet robust numerical flux schemes is the HLL scheme [33] which uses a two-wave model to approximate the solution to the exact Riemann problem at each face. Denoting $\boldsymbol{W}_L=\boldsymbol{W}_L\left(\boldsymbol{V}_{i+1/2}^L\right)$ and $\boldsymbol{W}_R=\boldsymbol{W}_R\left(\boldsymbol{V}_{i+1/2}^R\right)$, the HLL scheme can be expressed as,

$$\widehat{F}_{\mathrm{HLL}}=\frac{s_R F\left(\boldsymbol{W}_L\right)-s_L F\left(\boldsymbol{W}_R\right)+s_R s_L\left(\boldsymbol{W}_R-\boldsymbol{W}_L\right)}{s_R-s_L} \tag{14}$$

where s_L and s_R refer to the fastest left- and right-going signal speeds, respectively. Following the suggestion in Ref. [16], the signal speeds are computed as,

$$\begin{aligned} s_L &= \min\left[u_L-c_L,\quad \tilde{u}\left(u_L,u_R\right)-\tilde{c}\left(c_L,c_R\right), 0\right]\le 0 \\ s_R &= \max\left[u_R+c_R,\quad \tilde{u}\left(u_L,u_R\right)+\tilde{c}\left(c_L,c_R\right), 0\right]\ge 0 \end{aligned} \tag{15}$$

where $u=\boldsymbol{u}\cdot\boldsymbol{n}_f$ is the face normal velocity and $c=\sqrt{\gamma p/\rho}$ refers to the acoustic speed. Parameters with a tilde $(\sim)$ refer to the Roe-averages of the respective left- and right-sided values.

The HLLC flux scheme [34] is another widely used approximate Riemann solver. It is essentially the HLL scheme modified to allow the capturing of contact discontinuities exactly by introducing a third intermediate wave. Using the same definition of signal speeds, the HLLC scheme can be expressed as,

$$\widehat{F}_{\text{HLLC}} = \begin{cases} F(\boldsymbol{W}_L) + s_L(\boldsymbol{W}_{L*} - \boldsymbol{W}_L), & \text{if } s_* \geq 0 \\ F(\boldsymbol{W}_R) + s_R(\boldsymbol{W}_{R*} - \boldsymbol{W}_R), & \text{otherwise} \end{cases} \tag{16}$$

where $\boldsymbol{W}_{L*}$ and $\boldsymbol{W}_{R*}$ are respectively the left and right intermediate states separated by a contact discontinuity travelling at a velocity s_*. s_* can be computed as follows.

$$s_* = \frac{p_L - p_R + \rho_R(s_R - u_R)u_R - \rho_L(s_L - u_L)u_L}{\rho_R(s_R - u_R) - \rho_L(s_L - u_L)} \tag{17}$$

The intermediate states $\boldsymbol{W}_{L*}$ and $\boldsymbol{W}_{R*}$ can be determined using the following relationships.

$$\rho_{K*} = \rho_K \left(\frac{s_K - u_K}{s_K - s_*} \right) \quad \text{for } K = L, R \tag{18}$$

$$\boldsymbol{u}_{K*} = \boldsymbol{u}_K + (s_* - u_K)\boldsymbol{n}_f \quad \text{for } K = L, R \tag{19}$$

$$p_* = p_L + \rho_L(s_L - u_L)(s_* - u_L) = p_R + \rho_R(s_R - u_R)(s_* - u_R) \tag{20}$$

3.2 Characteristic fluxes (CF)

The VF approach is computationally cheaper and simpler to implement than the component-wise flux reconstruction approach. It performs well in smooth regions and even across contact discontinuities. However, it was observed to produce spurious oscillations near compressive regions and shocks where the characteristics coalesce. Higher order spatial reconstruction schemes, owing to their smaller numerical dissipation, allow such oscillations to persist longer and even grow in magnitude. Qiu and Shu [17] made a similar observation with respect to the component-wise approach. They demonstrated that performing a local characteristic decomposition and reconstructing the fluxes in characteristic space effectively eliminates the oscillations. This will be referred to as the characteristic flux (CF) approach in the present study.

A novel CF approach based on the HLL flux is designed to possibly reduce the numerical dissipation inherent in the conventional approaches which are usually based on Lax-Friedrich or Rusanov schemes. Characteristic flux approaches based on Lax-Friedrich or Rusanov flux schemes can be written in a split form,

$$F^{\pm} = \frac{1}{2}\left(\boldsymbol{F}_L \mp \lambda \boldsymbol{W}_L\right) \tag{21}$$

such that the numerical flux is the sum of the split fluxes, i.e. $\widehat{F} = F^{+} + F^{-}$. λ denotes the magnitude of the fastest signal speed which is taken to be $\Delta x/\Delta t$ and $\max\left(|s_R|, |s_L|\right)$ for Lax-Friedrich and Rusanov fluxes (also known as local Lax-Friedrich fluxes), respectively. Similarly, one can define a positive flux F^{+} and a negative flux F^{-} based on HLL scheme as follows such that $\widehat{F}_{\text{HLL}} = F^{+} + F^{-}$.

$$F^{+} = \frac{s_R}{s_R - s_L}\left[F\left(\boldsymbol{W}\right) - s_L \boldsymbol{W}\right], \qquad F^{-} = \frac{-s_L}{s_R - s_L}\left[F\left(\boldsymbol{W}\right) - s_R \boldsymbol{W}\right] \tag{22}$$

The fastest signal speeds are now calculated based on the owner and neighbour cell averages as shown below (compare Eq. (23) with Eq. (15)).

$$\begin{aligned} s_L &= \min\left[\overline{u_i} - \overline{c_i}, \quad \tilde{u}\left(\overline{u_i}, \overline{u_{i+1}}\right) - \tilde{c}\left(\overline{c_i}, \overline{c_{i+1}}\right), 0\right] \le 0 \\ s_R &= \max\left[\overline{u_{i+1}} + \overline{c_{i+1}}, \quad \tilde{u}\left(\overline{u_i}, \overline{u_{i+1}}\right) + \tilde{c}\left(\overline{c_i}, \overline{c_{i+1}}\right), 0\right] \ge 0 \end{aligned} \tag{23}$$

Having determined the signal speeds, the split fluxes $F^{\pm}$ are computed for all the cells that belong to the reconstruction stencil. The remaining procedure is identical to the CF approach based on Lax-Friedrich or Rusanov fluxes. First, the split fluxes are transformed to characteristic space using the left eigenvectors of the Jacobian $\partial_{\boldsymbol{W}} F$ computed based on a Roe-averaged state of the owner and neighbour states $\widetilde{\boldsymbol{W}}_{i+1/2} \equiv \widetilde{\boldsymbol{W}}\left(\overline{\boldsymbol{W}_i}, \overline{\boldsymbol{W}_{i+1}}\right)$ as shown below.

$$\mathcal{F}^{\pm} = \mathcal{L}\left(\widetilde{\boldsymbol{W}}_{i+1/2}\right) \bullet F^{\pm}$$

$$\text{where } \mathcal{L}\left(\boldsymbol{W}\right) = \frac{1}{2}\begin{bmatrix} b_2 + b_3 & -b_1 u - \dfrac{1}{c} & -b_1 v & -b_1 w & b_1 \\ 2\left(1 - b_2\right) & 2b_1 u & 2b_1 v & 2b_1 w & -2b_1 \\ -2v & 0 & 2 & 0 & 0 \\ -2w & 0 & 0 & 2 & 0 \\ b_2 - b_3 & -b_1 u + \dfrac{1}{c} & -b_1 v & -b_1 w & b_1 \end{bmatrix}, \tag{24}$$

$$b_1 = \frac{\gamma - 1}{c^2}, b_2 = \frac{b_1}{2}\left(u^2 + v^2 + w^2\right), b_3 = \frac{u}{c}$$

The velocity components u, v and w are defined locally with respect to the orientation of the face as,

$$u = \boldsymbol{u} \cdot \boldsymbol{n}_f, \quad v = \boldsymbol{u} \cdot \boldsymbol{t}_{f1}, \quad w = \boldsymbol{u} \cdot \boldsymbol{t}_{f2} \tag{25}$$

where the vectors $\boldsymbol{t}_{f1}$ and $\boldsymbol{t}_{f2}$ refer to unit tangential vectors to the face. The vectors form an orthonormal set, i.e. $\boldsymbol{t}_{f1} \cdot \boldsymbol{n}_f = \boldsymbol{t}_{f2} \cdot \boldsymbol{n}_f = \boldsymbol{t}_{f1} \cdot \boldsymbol{t}_{f2} = 0$.

Then, the characteristic positive flux $\mathcal{F}^+$ is reconstructed with a left bias and the characteristic negative flux $\mathcal{F}^-$ is reconstructed with a right bias using WENO scheme. Finally, the reconstructed characteristic fluxes are summed and projected back using the right eigenvectors of the same Jacobian as shown below.

$$\widehat{F}_{i+1/2} = \mathcal{R}\left(\widehat{\boldsymbol{W}}_{i+1/2}\right) \bullet \left[\left(\mathcal{F}^+\right)^L_{i+1/2} + \left(\mathcal{F}^-\right)^R_{i+1/2}\right]$$

$$\text{where } \mathcal{R}\left(\boldsymbol{W}\right) = \begin{bmatrix} 1 & 1 & 0 & 0 & 1 \\ u - c & u & 0 & 0 & u + c \\ v & v & 1 & 0 & v \\ w & w & 0 & 1 & w \\ h - uc & k & v & w & h + uc \end{bmatrix}, h = \frac{c^2}{\gamma - 1} + k, k = \frac{1}{2}\left(\boldsymbol{u} \cdot \boldsymbol{u}\right) \tag{26}$$

If one foregoes this local characteristic decomposition procedure (Eqs. (24) and (26)) and reconstructs the split fluxes $F^{\pm}$ instead of the characteristic fluxes $\mathcal{F}^{\pm}$, it is referred to as the component-wise flux approach. As evident from the procedure described above, the CF approach is computationally much more expensive than its VF counterpart, and hence, it would be very costly and time-consuming,

especially for large scale simulations. Therefore, it is crucial to develop an efficient hybrid flux approach.

3.3 Hybrid fluxes

In the hybrid flux approach, VF is applied everywhere except at certain critical areas where it may produce spurious oscillations. In these critical regions, CF is applied. In this study, the critical regions were identified using a shock sensor. Ducros, et al. [27] suggested a shock sensor of the following form which varies from 0 in weakly compressible regions to 1 near shocks. $\epsilon_s = 10^{-6}$ is a small number to prevent division by 0.

$$\Theta_{\text{Ducros}} = \frac{\left(\nabla \cdot \boldsymbol{u}\right)^2}{\left(\nabla \cdot \boldsymbol{u}\right)^2 + \left\|\nabla \times \boldsymbol{u}\right\|^2 + \epsilon_s} \tag{27}$$

Bhagatwala and Lele [26] modified it to be,

$$\Theta_{\text{BL}} = \frac{1}{2}\left[1 - \tanh\left(2.5 + A\frac{\nabla \cdot \boldsymbol{u}}{c/\Delta}\right)\right]\Theta_{\text{Ducros}} \tag{28}$$

where Δ refers to an appropriate length scale and A is an arbitrary constant suggested to be 10. Numerical experiments showed that a large Δ, say of the order of the length of the domain, causes Θ_{BL} to behave like a binary switch between 0 and 1 which was triggered even by small random perturbations. On the other hand, a small Δ, say of the order of ϵ_s, is tantamount to turning the sensor off altogether. Hence, Δ was taken to be a local mesh-dependent length scale computed as twice the maximum distance from the cell centre $\boldsymbol{x}_{\text{P}}$ to the centre of any of its bounding faces $\boldsymbol{x}_f$, i.e. $\Delta_{\text{P}} = 2\max\left(\left\|\boldsymbol{x}_{\text{P}} - \boldsymbol{x}_f\right\|\right)$. This choice of Δ was found to identify the critical regions satisfactorily without extending into the region of smooth flows. Finally, the shock sensor value at each face was taken to be the maximum of the owner and neighbour cell values, i.e. $\Theta_f = \max\left(\Theta_{\text{P}}, \Theta_{\text{N}}\right)$.

With the shock sensor computed at each face, the hybrid flux method is defined as,

$$\widehat{F}_f = \begin{cases} \widehat{F}_f^{\mathrm{VF}}, & \text{if } \Theta_f \le \Theta_{th} \\ \widehat{F}_f^{\mathrm{CF}}, & \text{if } \Theta_f > \Theta_{th} \end{cases} \tag{29}$$

where Θ_{th} is a user-specified threshold value. It is worthwhile to point out that the specific values of A and Θ_{th} are determined from a set of numerical tests discussed in the following section.

4 Results

4.1 Performance of HLL-based CF method

It is important to ascertain that the HLL-based CF method introduced earlier produces the correct solutions before proceeding to discuss the hybrid method itself. Hence, the proposed method is first compared with the popular Rusanov-based CF to assess its relative performance. The first test case is the 1D shock tube problem proposed by Sod [35] which is initialized as follows.

$$(\rho, u, p) = \begin{cases} (1.000, \ 0, \ 1.0), & x \le 0 \\ (0.125, \ 0, \ 0.1), & x > 0 \end{cases} \tag{30}$$

The problem was solved till $t = 0.2s$ on the domain $x \in [-0.5, 0.5]$ discretized uniformly into $N = 100$ cells. The results are shown in Figure 4 together with the exact solution (solid line).

Both CF methods produce monotone solutions without spurious oscillations for this shock tube problem. However, closer examination reveals that the HLL-based CF method captures a sharper shock and contact discontinuity, in addition to a slightly more accurate profile for the expansion fan as highlighted in Figure 4.

The second test case is the shock-entropy wave interaction problem introduced by Shu and Osher [36] which involves a Mach 3 shock impinging on a stationary region with sinusoidal density variations. The initial condition for this problem is given below in Eq. (31). The problem was solved until $t = 1.8s$ on the domain $x \in [-5, 5]$ discretized uniformly into $N = 200$ cells. The results are shown in Figure 5 together with the reference solution (solid line) computed on a 2000-cell grid.

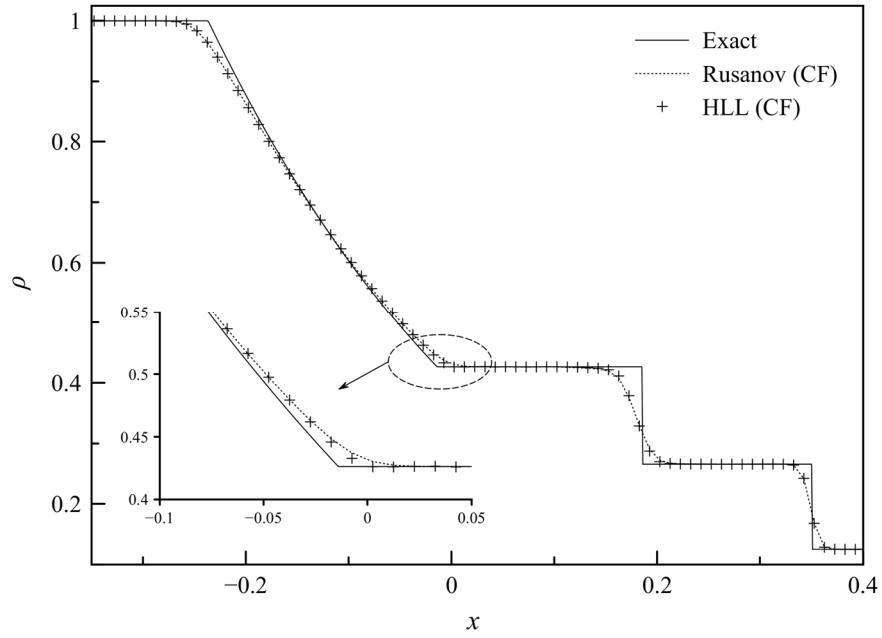

Figure 4: Comparison of CF methods for Sod' shock tube problem.

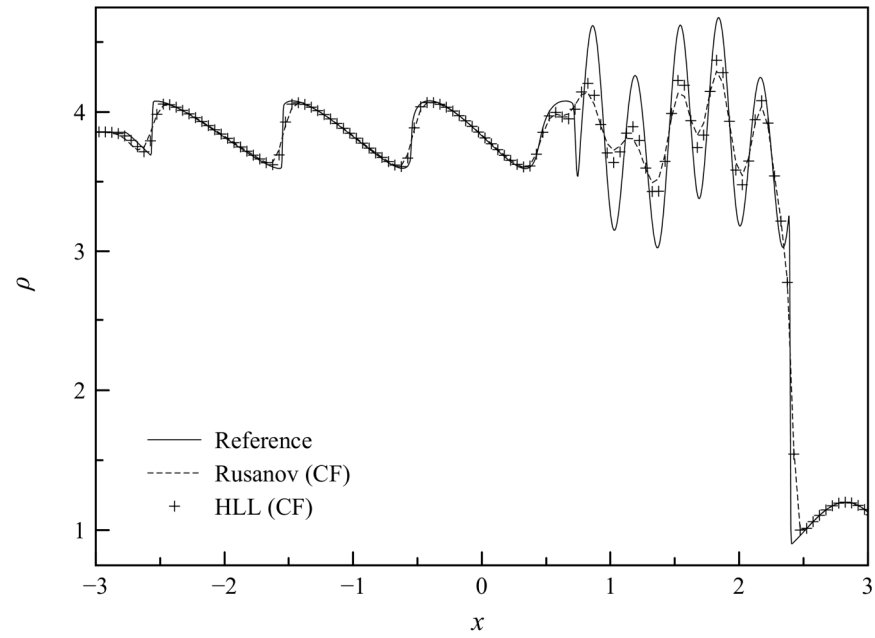

Figure 5: Comparison of CF methods for Shu-Osher problem.

$$(\rho, u, p) = \begin{cases} (3.857143, \quad 2.62937, \quad 10.3333), & x \le -4 \\ (1 + 0.2\sin(5x), \quad 0.000, \quad 1.000), & x > -4 \end{cases} \tag{31}$$

Similar to the shock tube problem, both CF methods perform well without spurious oscillations. However, more notably, the HLL-based CF method produces greater amplitudes for the short wavelength oscillations downstream of the shock compared to the Rusanov-based CF method which

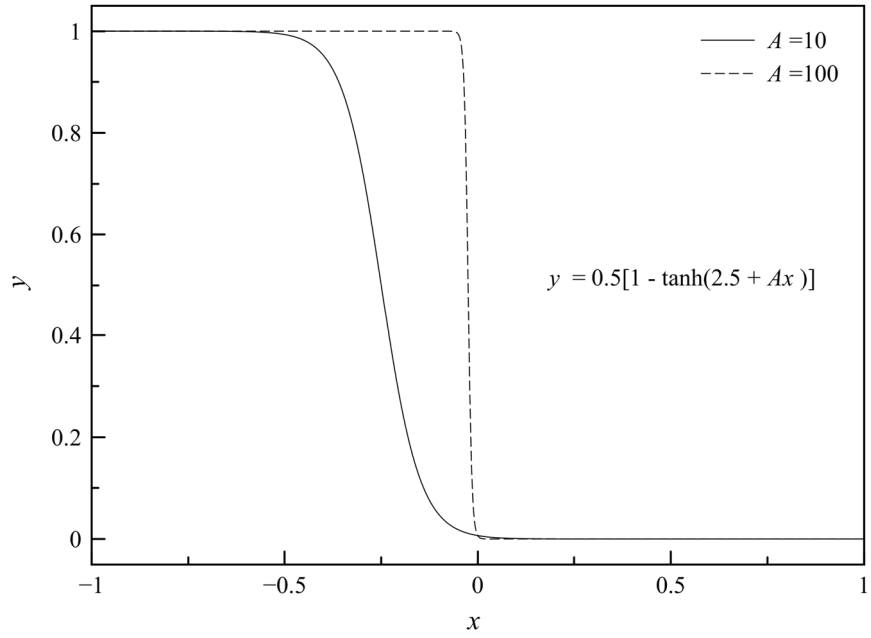

Figure 6: Effect of parameter A in shock sensor.

clearly illustrates that, being less dissipative, the HLL-based CF method achieves better accuracy in the smooth regions. The results from these two test cases lend strong support for the use of the HLL-based CF method in all subsequent investigations on the hybrid scheme.

4.2 Effect of parameter A in shock sensor

The effectiveness of the hybrid method defined in Eq. (29) depends largely on the ability of the shock sensor to accurately identify the critical regions across where CF needs to be applied. During preliminary tests, it was observed that using the suggested value of A=10 in Eq. (28) did not result in oscillation-free solution. Therefore, the value of A was increased to 100 so that the sensor became sensitive, not only to strong shocks, but to the mildly compressive regions as well (see Figure 6). The effect of modifying parameter A will be demonstrated in this section. Note that the results presented in this section were obtained by reconstructing the primitive variables $\boldsymbol{V} = \left[\rho, \boldsymbol{u}, p\right]$.

The two 1D test cases described in the previous section were used to study the effect of parameter A. Both HLL and HLLC schemes were used and the threshold value was set to $\Theta_{th} = 0.1$. The final density profiles (+) and shock sensor values (red dotted line) are plotted in Figures 8 and 9 for Sod's shock tube problem and Shu-Osher problem, respectively.

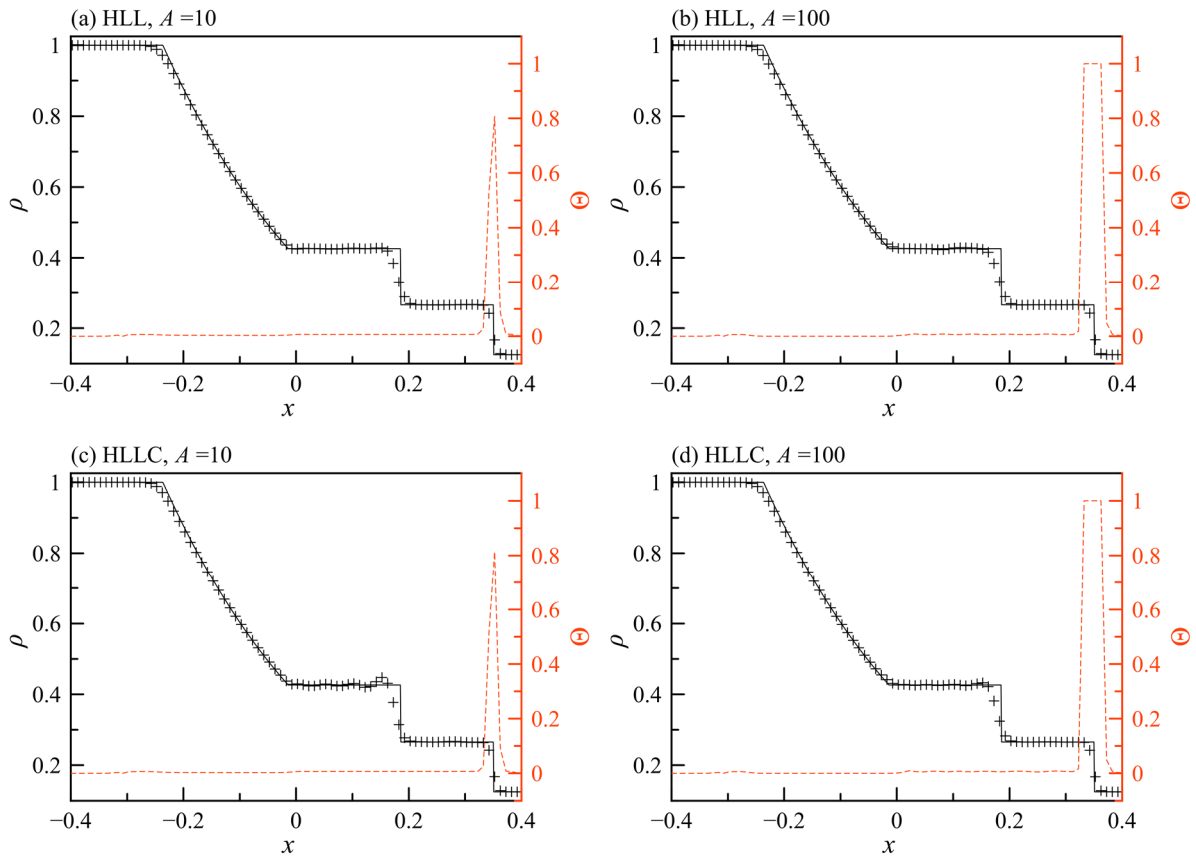

Figure 7: Effect of parameter A for Sod's shock tube problem.
Solid line: exact solution, +: hybrid method, red dotted line: shock sensor

As mentioned earlier, increasing A makes the sensor more sensitive to compressive regions. As a result, using $A=100$ produces greater values of Θ and affects a wider region near the shock compared to using $A=10$. This is evident comparing Figures 7(a) and (c) with their counterparts Figures 7(b) and (d), where narrower peaks value with decreased magnitude were observed for $A=10$. Moreover, the effect of increasing A has little effect on the results for Sod's problem when using the HLL scheme (compare Figures 7(a) and (b)). On the other hand, noticeable improvement is obtained for the HLLC scheme in the vicinity of the contact discontinuity near $x=0.2$. It is clear from Figure 7(c) that using $A=10$ is inadequate in preventing the development of spurious oscillations due to a smaller critical region identified and thus evaluated with CF. Comparing this with Figure 7(d), increasing the parameter to $A=100$ has significantly attenuated the spurious oscillations, in particular, to the left of the contact discontinuity. Interestingly, by applying CF in a wider region enveloping the shock, the hybrid scheme effectively suppresses the development of spurious oscillations.

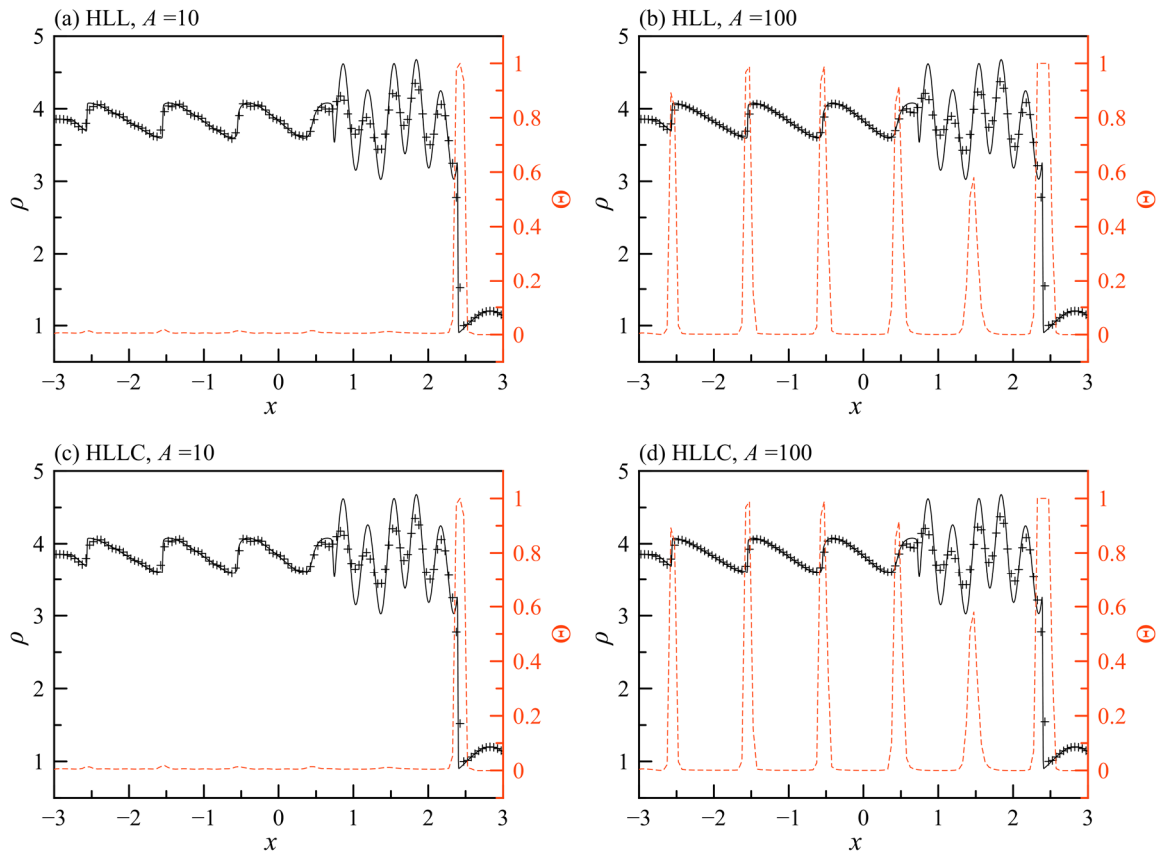

Figure 8: Effect of parameter A for Shu-Osher problem.
Solid line: reference solution, +: hybrid method, red dotted line: shock sensor

For the Shu-Osher problem, both HLL and HLLC schemes produce nearly identical results. In all cases, CF is applied across the strong Mach 3 shock near $x = 2.4$, regardless of the value of A since $\Theta \approx 1$, though it is noteworthy that the critical region around the shock is wider when using $A = 100$. Yet, all four cases result in similar amplitudes for the short wavelength oscillations between $x = 0.5$ and 2. Conversely, it can be observed from Figures 8(a) and (c) that the density profiles exhibit small spurious oscillations along the long slanting legs of the N-waves for $A = 10$. Close examination of the values of Θ in Figures 8(a) and (c), reveals tiny bumps near the short rising legs of the N-waves, indicating that these regions are mildly compressive. Nonetheless, CF is not activated across the N-waves as the value of Θ is smaller than the threshold Θ_{th}. On the other hand, when A is increased to 100, the shock sensor becomes more sensitive to these mildly compressible regions (i.e. $\Theta > \Theta_{th}$) and consequently, the N-wave oscillations are essentially eliminated as evident from Figures 8(b) and (d).

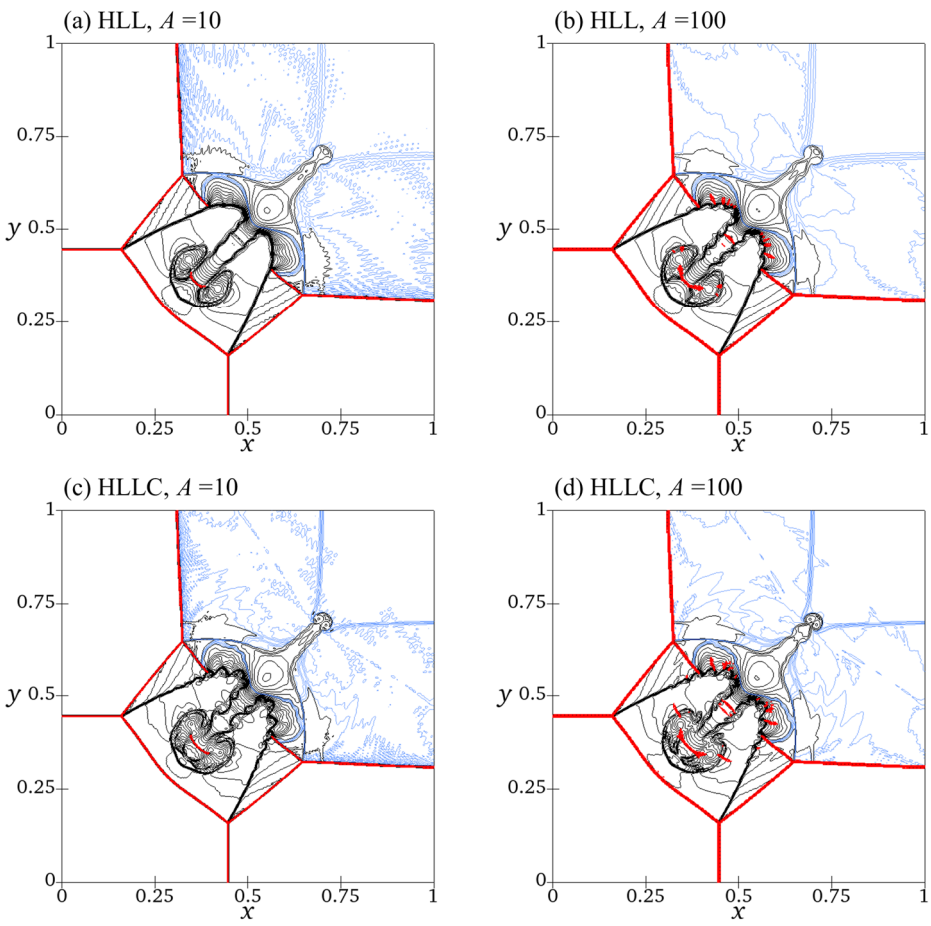

Figure 9: Effect of parameter A for interaction of planar shocks $\left(\Theta_{th}=0.1\right)$.
Critical areas using CF highlighted in red.

Moving beyond 1D problems, the third test case is a 2D Riemann problem involving the interactions of four planar shocks proposed by Lax and Liu [37]. The initial condition for this problem consists of four constant states separated by normal shocks as given below in Eq. (32).

$$\left(\rho,u,v,p\right)=\begin{cases}\underline{x<0.7,\ y\geq 0.7} & \underline{x\geq 0.7,\ y\geq 0.7}\\ \left(0.5323,1.206,0,0.3\right) & \left(1.5,0,0,1.5\right)\\ \\ \underline{x<0.7,\ y<0.7} & \underline{x\geq 0.7,\ y<0.7}\\ \left(0.138,1.206,1.206,0.029\right) & \left(0.5323,0,1.206,0.3\right)\end{cases} \tag{32}$$

The problem was solved until $t=0.6s$ on the domain $x\times y\in\left[0,1\right]\times\left[0,1\right]$ discretized uniformly using cells of width $\Delta x=\Delta y=1/500$. Neumann boundary conditions were used on all four sides. Once again, both HLL and HLLC flux schemes were used. On top of two different value for parameter A, two

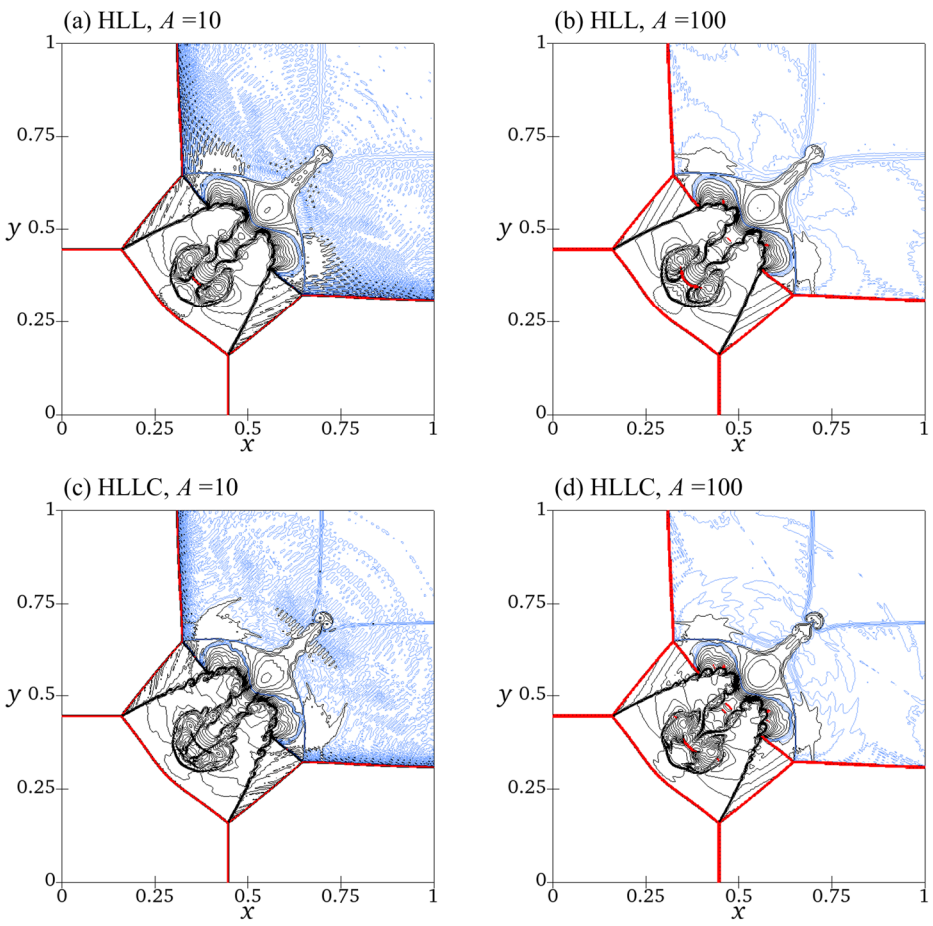

Figure 10: Effect of parameter A for interaction of planar shocks $\left(\Theta_{th} = 0.9\right)$. Critical areas using CF have been highlighted in red.

distinct threshold values, 0.1 and 0.9, were used to investigate the combined effects of A and Θ_{th}. The final density contours for $\Theta_{th} = 0.1$ and 0.9 are shown in Figures 9 and 10, respectively. In these figures, the black lines are 33 evenly-spaced density contours from 0.15 to 1.75 while the light blue lines are 4 evenly-spaced density contours from 1.46 to 1.49 to accentuate the noise generated in the top-right region, and moreover, the critical areas identified by the shock sensor where CF was applied have been highlighted in red in the figures.

As seen from Figure 9, significant amount of numerical noise is generated from the shocks, evidenced by the oscillatory contour lines spanning across the top-right region of the domain. Comparing Figures 9(a) and (c) with Figures 10(a) and (c), it is apparent that the problem becomes more severe when Θ_{th} is increased since CF will be applied in smaller regions near shocks. When A is increased to 100, however, the noise is reduced significantly. Moreover, comparing Figures 9(b) and (d) with Figures

10(b) and (d), only minor differences can be observed in the top-right region with the increase in Θ_{th} from 0.1 to 0.9. This is a favourable trait since the results are not too sensitive to the choice of Θ_{th}. Unlike the Shu-Osher problem earlier, the choice of numerical flux scheme has noticeable effects for this problem. For any combination of A and Θ_{th}, HLLC scheme is able to capture more vigorous and prominent roll-ups, both in terms of number and size of vortices, along the slip line. This trend is observed in all 2D cases tested and should come as no surprise since the HLLC scheme has been designed to capture contact discontinuities exactly.

To briefly summarize, it can be established with good confidence from the 1D and 2D test cases above that increasing A from 10 to 100 prevents spurious oscillations reasonably well and does not affect the resolution of the hybrid method for a given numerical flux scheme. Based on these observations, the parameter A was set to 100 for subsequent simulations, and also threshold values of $\Theta_{th} = 0.1$ and $\Theta_{th} = 0.9$ were found to perform well for 1D and 2D problems, respectively.

4.3 Effect of the choice of reconstructed variables

Although the choice of variables had little influence on the results for 1D cases, the effects on 2D cases become significant in the extent of details captured for the roll-ups along slip lines. To demonstrate this effect clearly, a different 2D Riemann problem is considered here. This problem proposed by Lax and Liu [37] involves the interaction of four planar discontinuities. The initial condition for this problem is given below.

$$(\rho, u, v, p) = \begin{cases} \underline{x < 1,\ y \geq 1} & \underline{x \geq 1,\ y \geq 1} \\ (2, 0.75, 0.5, 1) & (1, 0.75, -0.5, 1) \\ \underline{x < 1,\ y < 1} & \underline{x \geq 1,\ y < 1} \\ (1, -0.75, 0.5, 1) & (3, -0.75, -0.5, 1) \end{cases} \tag{33}$$

Notice that the pressure is uniform everywhere and that only the density and velocity component tangential to the discontinuity change across each discontinuity. Upon initialization, Kelvin-Helmholtz instabilities form along the contact discontinuities, giving rise to roll-ups of a series of vortices. In the

present investigation, the problem was solved till $t = 1.6s$ on the domain $x \times y \in [0, 2] \times [0, 2]$ discretized uniformly using cells of width $\Delta x = \Delta y = 1/240$. Neumann boundary conditions were used on all four sides. The results are shown in Figure 11 using 24 evenly-spaced density contours from 0.14 to 2.44. The results computed entirely using CF is shown in Figure 11(e) together with the labelling for the four shear layers (S1, S2, S3 & S4), as a single scheme reference.

All the methods capture the general structure of the solution accurately without any noticeable spurious oscillations, corroborating to the fact that the present hybrid method coupled with the modified shock sensor is effective in eliminating spurious numerical oscillations. Nevertheless, the amount of details captured for the roll-ups along the shear layers differ notably. Most strikingly, using conservative variables $\boldsymbol{W}$ results in the formation of significantly more roll-ups (Figures 11(b) and (d)) along all shear layers. In contrast, using the primitive variables $\boldsymbol{V}$ only, which has worked satisfactorily well thus far, results in merely a pair of roll-ups along shear layers S2 and S4, let alone the absence of roll-ups along shear layers S1 and S3. Interestingly, the trends are the same for both HLL and HLLC schemes, even though the latter is deigned to achieve improved accuracy and resolution along slip lines (i.e. more roll-ups along the shear layers, as manifested in the previous 2D Riemann problem in Figures 9 and 10). Referring back to the reference results obtained using CF alone, the shear layer roll-ups appear to correspond well with those obtained from the hybrid method using primitive variables $\boldsymbol{V}$. However, it must be pointed out that there exist slight differences between the two. For instance, shear layer S1 starts to show signs of instability with obvious waviness when using CF alone (Figure 11(e)) whereas it remains quite smooth when using the hybrid method (Figure 11(a) and (c)).

Conventionally, the extent of details captured is viewed as a measure of the numerical dissipation of the spatial reconstruction scheme and/or the numerical flux scheme. While this is certainly true, one should also consider the mathematical validity of the solution for the complete story. In an attempt to further investigate this curious observation a new test case was devised with the following initial condition.

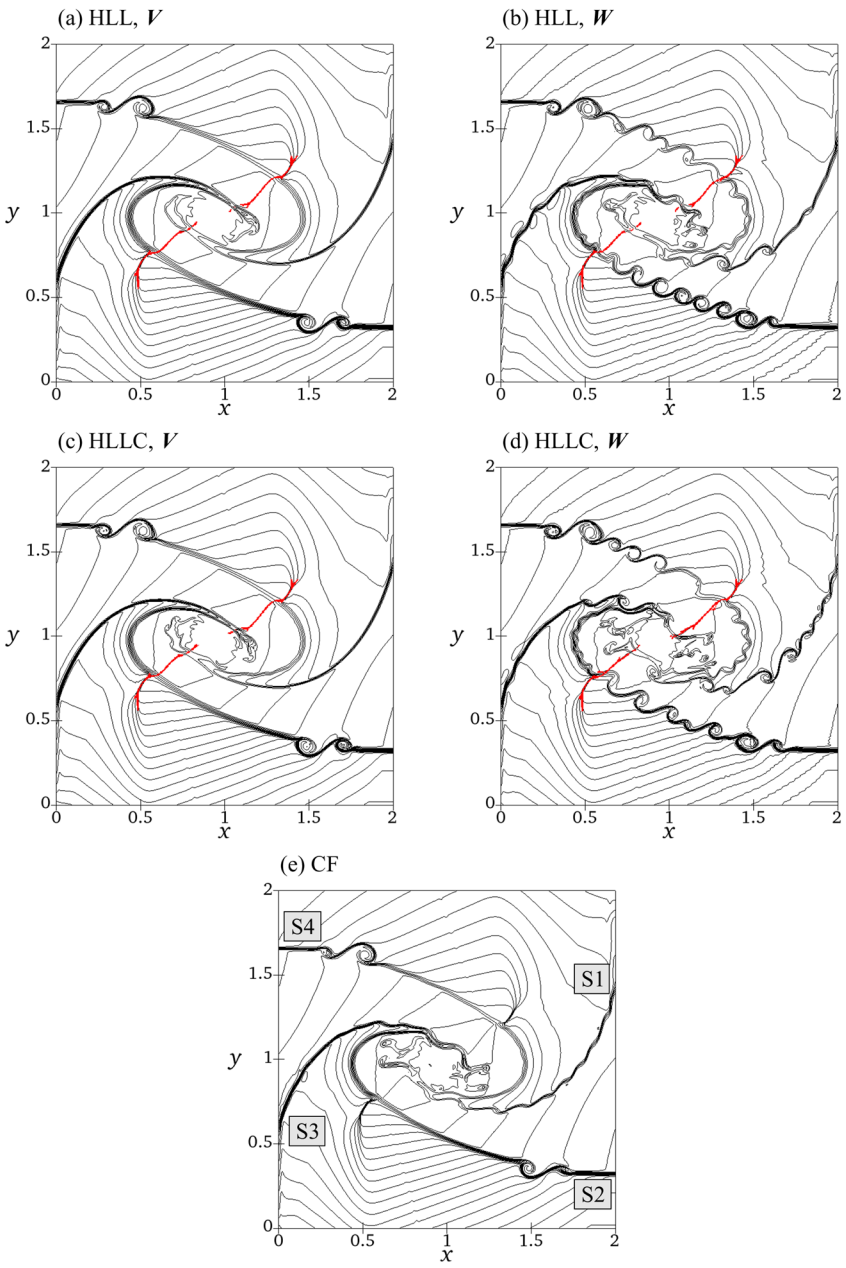

Figure 11: Effect of choice of reconstructed variables for interaction of planar contact discontinuities problem. Critical areas using CF have been highlighted in red.

$$(\rho, u, v, p) = \begin{cases} \big(1+0.5\cos(\pi x)\cos(\pi y),\quad 1.0,\quad 0,\quad 2.5\big), & |y| \le 0.25 \\ \big(1-0.5\cos(\pi x)\cos(\pi y),\quad 0.5,\quad 0,\quad 2.5\big), & |y| > 0.25 \end{cases} \tag{34}$$

It is simply an advection problem with three streams of gas separated by contact discontinuities. The problem was solved till $t = 2s$ on the domain $x \times y \in [-0.5, 0.5] \times [-0.5, 0.5]$ discretized uniformly into cells of width $\Delta x = \Delta y = 1/240$. Periodic boundary conditions were applied on all four sides. As such, the exact solution to this problem is simply the initial condition given in Eq. (34). The results are shown

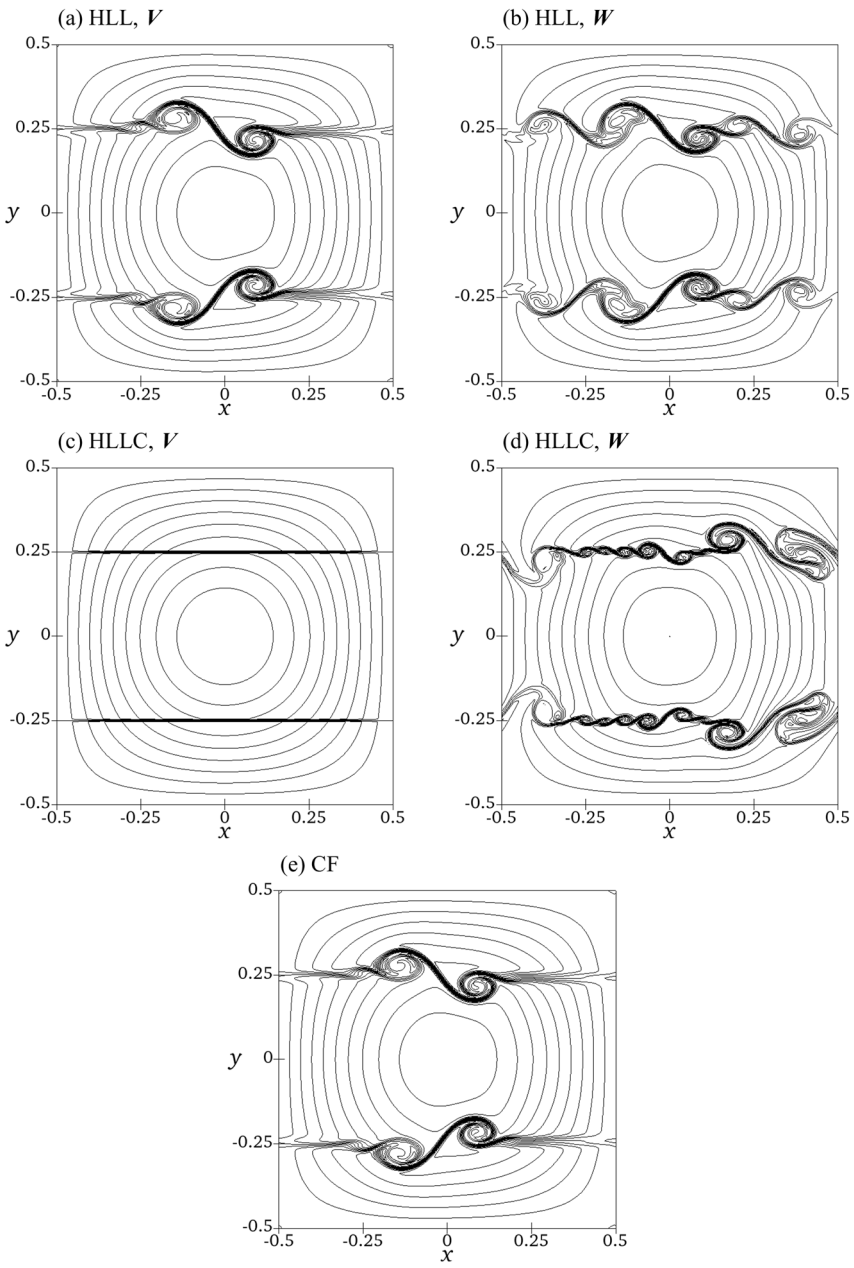

Figure 12: Effect of choice of reconstructed variables for 2D advection problem.

in Figure 12 using 21 evenly-spaced density contours from 0.5 to 1.5. Since there are no shocks present, the solutions were effectively computed using the respective VF methods only. For consistency and comparison, the case was also simulated entirely using CF (Figure 12(e)).

It can be seen from Figure 12 that only the HLLC scheme using primitive variables manages to reproduce the exact solution. The remaining methods, including CF, generate roll-ups along the contact discontinuities. The reason behind such roll-ups is two-fold: the inability of the numerical flux scheme to capture an isolated contact discontinuity exactly and the numerical errors caused by deriving the

primitive quantities (pressure and velocity) by reconstructing the conservative variables (momentum and total energy). Being unable to capture an isolated contact discontinuity exactly, both the HLL scheme and CF smear and destabilize the interface, leading to the observed roll-ups as seen in Figures 12(a) and (e). As noted by Karni [38], the numerical diffusion of conservative variables across the contact discontinuity produces pressure and velocity fluctuations which induce the formation of such roll-ups. In a similar vein, Johnsen and Colonius [39] have pointed out that, deriving pressure by reconstructing the conservative variables results in incorrect values being used in the numerical flux computation. The results obtained for the present case corroborates with their findings since even when using HLLC, which is capable of capturing an isolated contact discontinuity exactly as evident from Figure 12(c), the use of conservative variable reconstruction causes the solution to deviate from the exact solution as shown in Figure 12(d).

To summarize, use of a numerical flux scheme that is incapable of resolving an isolated contact discontinuity exactly and the reconstruction of conservative variables result in two different but related sources of numerical instability along slip lines, which both manifest essentially as large-scale roll-ups. The results obtained from HLL scheme with conservative variable reconstruction bears the trademark of both sources of instability. The two large roll-ups between $-0.25 < x < 0.15$ correspond to the former source of instability since they are also observed in Figure 12(a) while the two prominent roll-ups at both ends $x \approx \pm 0.4$ corresponding to the latter since similar features are observed in Figure 12(d).

More importantly, these results suggest that sufficient cautions have to be taken before judging a method depending on the number and size of roll-ups it produces in a given numerical test since such roll-ups may stem from numerical instabilities. On one hand, it is desirable to obtain numerical solutions as close to the theoretically exact solution as possible. In this regard, the HLLC scheme with primitive variable reconstruction is undeniably the most accurate. On the other hand, realistically speaking, no physical flow is free from disturbances. In this regard the numerical instabilities are somewhat analogous to the physical disturbances which destabilize the shear layer causing it to roll up. As a result, one may be inclined to view the formation of roll-ups to be closer to reality. However, in the absence validations using experimental results, this argument is not completely sound since one does not know

what the true reality is. Therefore, it is not possible to conclude that one set of variables is better than another from the results obtained for the planar discontinuities interaction problem (Figure 11). Nonetheless, based the results for the newly devised 2D advection case, the hybrid method using the HLLC scheme primitive variable reconstruction is still recommended.

4.4 Additional numerical tests

4.4.1 Shock instability problem (Quirk test)

It is well-known that the HLLC scheme is susceptible to a multi-dimensional shock instability problem commonly known as the 'carbuncle problem' [40]. Quirk [41] proposed a simple 2D problem to test whether a flux scheme suffers from this affliction. It involves a Mach 6 shock propagating into quiescent gas simulated on a perturbed grid to trigger the instability. The simulation domain is a rectangle $x \times y = [0, 800] \times [-10, 10]$ discretized uniformly into cells of width $\Delta x = \Delta y = 1$. The horizontal centerline $y = 0$ is perturbed in the following manner.

$$y_{i,\text{mid}} = \begin{cases} -10^{-6}, & \text{if } i \text{ is odd} \\ +10^{-6}, & \text{if } i \text{ is even} \end{cases} \tag{35}$$

The simulation was initialized as follows with the shock initially positioned at $x = 10$.

$$(\rho, u, v, p) = \begin{cases} (5.6283, 5.7514, 0, 41.8333) & x \le 10 \\ (1.000, \quad 0.000, \quad 0, \quad 1.000) & x > 10 \end{cases} \tag{36}$$

The case was run till $t = 105s$ using HLLC scheme with and without CF near shocks. The results are shown in Figure 13 using 16 evenly-spaced density contours from 1.25 to 5. It is clear from Figure 13(b) that the hybrid method does not suffer from the shock instability problem.

4.4.2 Forward-facing step problem

The Mach 3 forward-facing step problem [42] was solved on the domain $[x, y] \in [0, 3] \times [0, 1]$ discretized uniformly using cells of width $\Delta x = \Delta y = 1/160$. The 0.2 units high step extends to the right from $x = 0.6$. Inflow and outflow (Neumann) boundary conditions were specified at the left and right

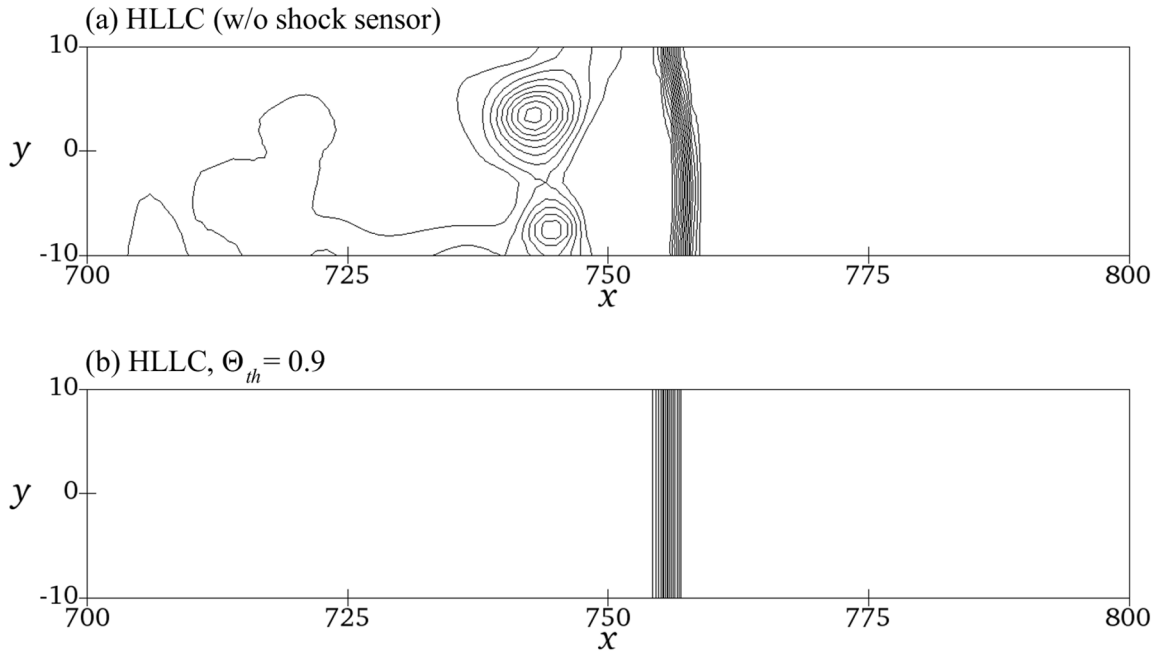

Figure 13: Comparison of HLLC scheme (a) without CF and (b) with CF near shock for Quirk test.

boundaries, respectively. All other boundaries were set to be reflective. The special treatment suggested by Woodward and Colella [43] was applied at the step corner to eliminate the effects of the unphysical 'boundary layer' that would otherwise corrupt the solution. The problem was initialized with the conditions given in Eq. (37) and it was simulated till $t = 3s$ using both the fully CF solver and the VF/CF hybrid solver. The final density contours are shown in Figure 14 and the critical areas where CF was used in the hybrid solver is highlighted in red in Figure 14(b).

$$\left(\rho, u, v, p\right)_0 = \left(1.4, 3, 0, 1\right) \tag{37}$$

It is evident from the results that the hybrid VF/CF solver is able to capture the flow accurately without producing any notable spurious oscillations compared to the fully CF solver despite the fact that CF is applied at only a small portion of the domain. Moreover, the hybrid VF/CF solver results in more well-defined roll-ups emanating from the triple point thanks to the contact capturing ability of the HLLC flux scheme.

4.4.3 Shock/shear layer interaction problem

The shock/shear layer interaction problem [44] was solved on the domain $\left[x, y\right] \in \left[0, 200\right] \times \left[-20, 20\right]$

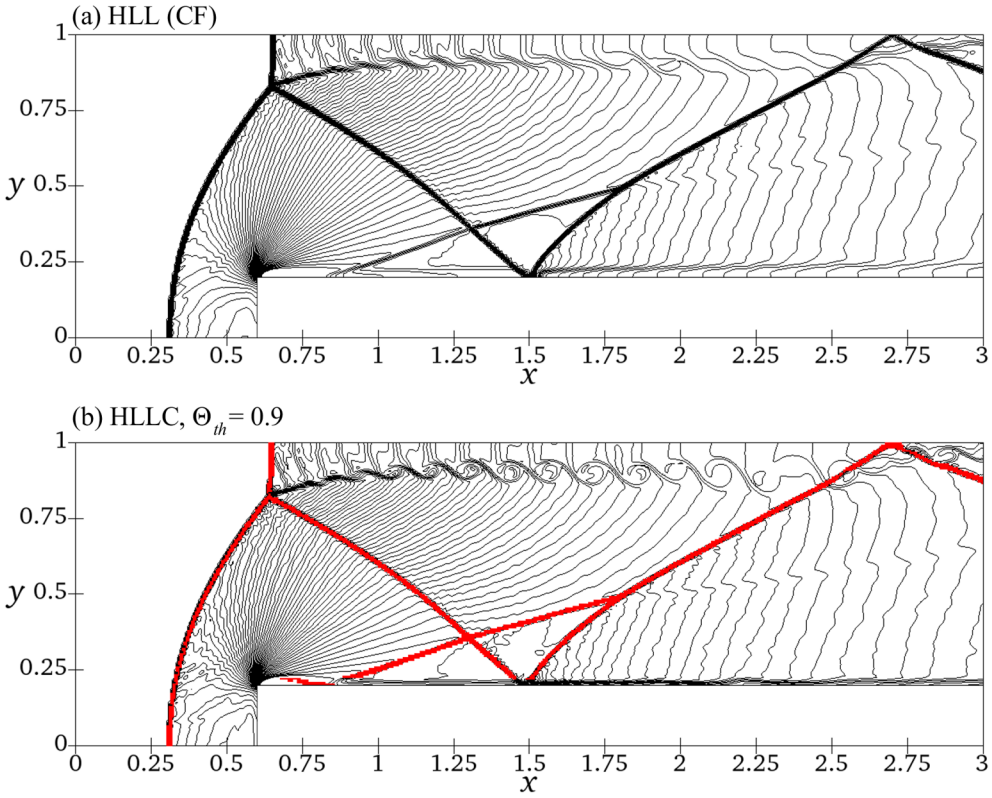

Figure 14: Comparison of (a) fully CF and (b) VF/CF hybrid solver for Mach 3 forward-facing step problem. Critical areas using CF have been highlighted in red.

discretized uniformly into cells of width $\Delta x = \Delta y = 2.5$. The problem was initialized with the following condition.

$$\rho = \begin{cases} 1.6374, & y > 0 \\ 0.3626 & y \le 0 \end{cases}, \quad (u, v, p) = \left(2.5 + 0.5\tanh(y), 0, 0.3327\right) \tag{38}$$

Outflow and reflective boundary conditions were specified at the right and bottom boundaries, respectively. The top boundary was specified with following the post-shock values.

$$\left(\rho, u, v, p\right)_{top} = \left(2.1101, 2.9709, -0.1367, 0.4754\right) \tag{39}$$

Lastly, the left boundary was set to the initial values given in Eq. (38) except for the y velocity component v which was specified as

$$v_{left} = 0.05e^{-0.1y^2}\left[\cos\left(2\pi t/T\right) + \cos\left(4\pi t/T + \pi/2\right)\right], \qquad T = \frac{\lambda}{u_c} \tag{40}$$

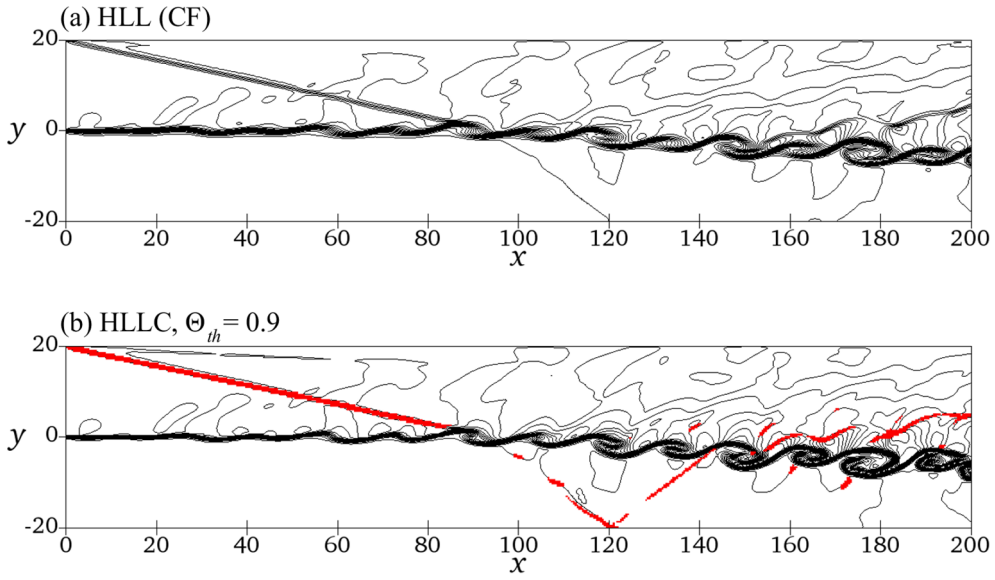

Figure 15: Comparison of (a) fully CF and (b) VF/CF hybrid solver for shock/shear layer interaction problem. Critical areas using CF have been highlighted in red.

where $\lambda = 30$ refers to the wavelength and the $u_c = 2.68$ refers to the convective velocity. The problem was simulated till $t = 120s$ using both the fully CF solver and the hybrid VF/CF solver. The final density contours are shown in Figure 15 and the critical areas have been highlighted in red.

Similar to the previous case, the hybrid VF/CF solver is able to capture the flow accurately with little to no spurious oscillations compared to the fully CF solver. In addition, the hybrid solver is able to capture the shear layer vortices with lesser numerical diffusion compared to the fully CF solver.

4.4.4 Double Mach reflection problem

The double Mach reflection (DMR) problem [43] involves a Mach 10 oblique shock impinging on a ramp. The problem was solved using an alternative setup proposed by the authors in Ref. [45] that allows exact tracking of the oblique shock as it traverses across the top boundary without introducing undesirable numerical artefacts into the solution. In this alternative setup, the computational domain $[x, y] \in [-1, 3] \times [0, 1]$ was discretized uniformly using cells of width $\Delta x = \Delta y = 1/240$ and the ramp extends from $x = 0$ to the right along the bottom boundary. The problem was initialized with the exact pre- and post-shock conditions as follows.

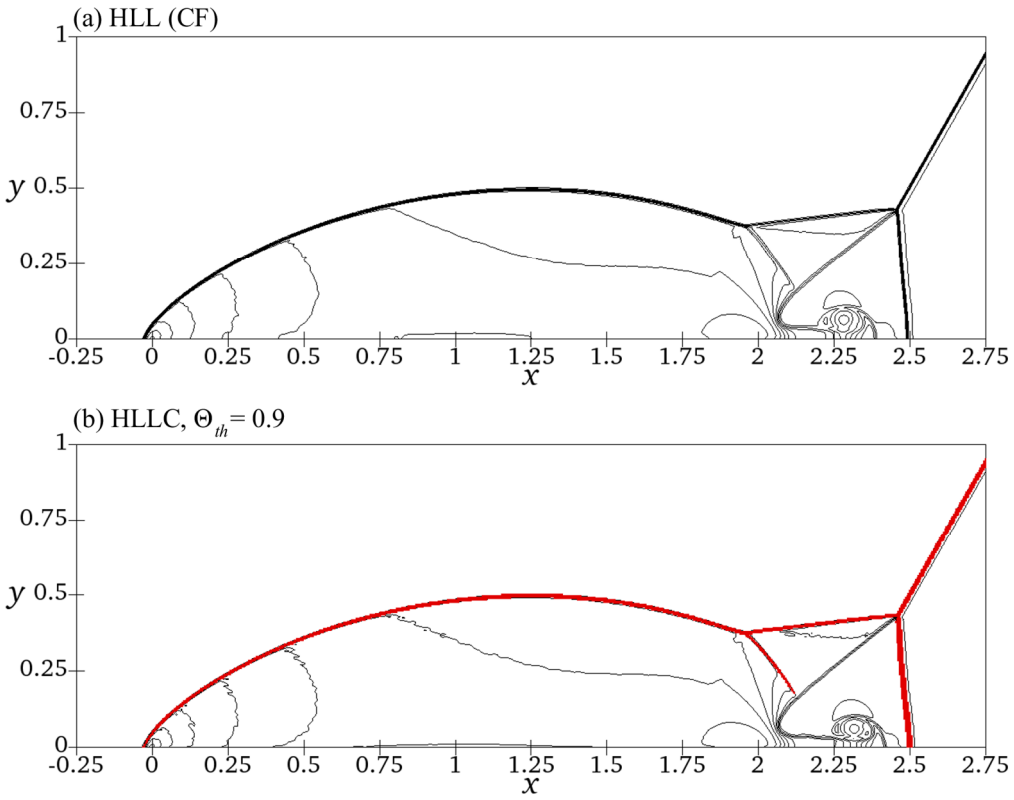

Figure 16: Comparison of (a) fully CF and (b) VF/CF hybrid solver for double Mach reflection problem. Critical areas using CF have been highlighted in red.

$$(\rho, u, v, p)_0 = \begin{cases} (1.0, 0, 0, 1.0), & y < (x - x_s)\tan\theta \\ (8.0, -8.25\cos\theta, -8.25\sin\theta, 116.5), & y \geq (x - x_s)\tan\theta \end{cases} \tag{41}$$

The shock was initialized to intersect the bottom boundary at $x_s = -0.9$ which is a short distance to the left of the ramp. The oblique shock makes an angle of $\theta = \tan^{-1}(7/4) \approx 60.25°$ with respect to the horizontal axis. From $t = 0$ to $t = 0.08$, the shock was allowed to propagate without obstruction until it reached the foot of the ramp $(x = 0)$. Then, the domain downstream (left) of the shock was re-initialized with the post-shock values before continuing the simulation until $t = 0.27$. The exact pre- and post-shock conditions were specified at the right and left boundaries, respectively. Reflective boundary condition was applied along the ramp portion of the bottom boundary. The problem was solved using both solvers and the final density contours are shown in Figure 16.

It is evident that both solvers are able to capture the intricate flow features accurately. The results appear nearly identical to each other with one key difference: the slip line and the wall-attached jet captured

by the VF/CF hybrid method are sharper compared to those captured by the fully CF method possibly due to the use of the HLLC scheme. The HLLC scheme is known to result in a kinked Mach stem [41], yet another manifestation of the shock instability problem mentioned earlier, for the DMR problem. However, the hybrid method produces no unphysical kinks along the Mach stem that intersects the bottom boundary at $x = 2.5$ as the CF method is applied around shocks. This test case exemplifies the advantage of using a hybrid method in overcoming the weaknesses of the one method with the strengths of another.

4.5 Computational savings

The VF/CF hybrid method based on the modified shock sensor is undoubtably faster compared to a pure CF method for all the cases tested thus far. The VF approach is faster than the CF approach due to two main reasons. Firstly, in the VF approach, fewer third order polynomial reconstructions are performed per face since the same quantities (variables) are reconstructed from both sides of the face. In addition, the computation of the smoothness indicators based on the polynomial coefficients can be optimized in the VF approach to bring about further savings. Secondly, the CF approach requires the fluxes and characteristic projections to be computed for *all* cells in the stencil before performing the WENO reconstructions. In contrast, the flux computation in the VF approach is straightforward.

Naturally, the computational savings vary from case to case depending on the fraction of faces where CF is applied as well as computational platform and programming implementation. Nevertheless, a quantitative comparison of the speedup achieved for the two 1D cases, Sod's shock tube problem and Shu-Osher problem, is provided in Table 1. Note that the results are shown for HLLC scheme using primitive variable reconstruction with $\Theta_{th} = 0.1$ based on the *total* computation time which includes the computation of the shock sensor and the switching operations. Notice that the speedup plateaus at about 4.1 times at the higher resolutions as CF gets activated in ever smaller proportions of the faces and VF is applied at nearly all faces. Similar speedups were observed across all 2D cases consistently. Although no 3D cases were investigated, it can be safely argued that the proposed hybrid method will bring about

Table 1: Relative speedup achieved using VF/CF hybrid method compared to a pure CF method for 1D problems

N	Speedup	
	Sod's shock tube problem	Shu-Osher problem
200	3.30	3.39
400	3.72	3.76
800	4.00	3.99
1600	4.11	4.08
3200	4.14	4.14

similar savings, especially for large scale simulations in which the shocks occupy only a small fraction of the domain.

5 Conclusions

In this paper, a hybrid method for solving Euler equations compatible with high order schemes was presented along with key pointers for implementation in OpenFOAM®. A seventh order WENO scheme was used for spatial reconstruction. The method switches from a simple variable-based flux (VF) approach to the more expensive characteristic flux (CF) approach depending on the value of a shock sensor. The Bhagatwala-Lele shock sensor was modified in order to make it more sensitive to mildly compressible regions. The modified shock sensor was demonstrated to be effective in identifying the critical areas where CF needs to be applied. A novel HLL-based CF approach was proposed, and it has been shown to produce accurate non-oscillatory solutions with lesser numerical dissipation compared to the popular Rusanov-based CF approach. The VF approach was implemented with the HLL and HLLC schemes using both primitive and conservative variable reconstructions. The effect of the choice of reconstructed variables was also investigated. It was concluded that primitive variable reconstruction with HLLC scheme delivers the best performance for capturing contact discontinuities. Finally, it was shown that the hybrid method using HLLC scheme does not suffer from the carbuncle phenomenon.

The hybrid method resulted in considerable computational savings for all the cases tested. The additional cost of computing the shock sensor and performing the switch using if-else logic operations is small price to pay for the huge speedup in computation time obtained.

6 Acknowledgements

The authors gratefully acknowledge the support for the present work by Singapore Ministry of Education AcRF Tier-2 grant (MOE2014-T2-1-002) and support for the first author through Graduate Research Officer scholarship from School of Mechanical and Aerospace Engineering, Nanyang Technological University, Singapore. The authors would also like to thank Prof Chan Wai Lee for taking his time to discuss certain aspects of the numerical methods which had a major influence on the direction of this paper. The computational work for this article was partially performed on resources of the National Supercomputing Centre, Singapore (https://www.nscc.sg).

7 Appendix A

For each sub-stencil j, the fourth order polynomial approximation $\left(\rho_{i+1/2}\right)_j$ and the three polynomial coefficients $a_{k,j}$ are determined from the cell averages in that sub-stencil using is a 4×4 reconstruction matrix $\mathbf{R}_j$ as shown below.

$$\begin{pmatrix} \rho_{i+1/2} \\ a_1 \\ a_2 \\ a_3 \end{pmatrix}_j = \mathbf{R}_j \begin{pmatrix} \overline{\rho_{i-3+j}} \\ \overline{\rho_{i-2+j}} \\ \overline{\rho_{i-1+j}} \\ \overline{\rho_{i+j}} \end{pmatrix} \tag{A1.1}$$

For the case of uniform cells, the sub-stencil reconstruction matrices are given by:

$$\mathbf{R}_0 = \begin{bmatrix} -\frac{1}{4} & \frac{13}{12} & -\frac{23}{12} & \frac{25}{12} \\ -\frac{11}{12} & \frac{15}{4} & -\frac{23}{4} & \frac{35}{12} \\ -\frac{3}{4} & \frac{11}{4} & -\frac{13}{4} & \frac{5}{4} \\ -\frac{1}{6} & \frac{1}{2} & -\frac{1}{2} & \frac{1}{6} \end{bmatrix}$$

$$\mathbf{R}_1 = \begin{bmatrix} \frac{1}{12} & -\frac{5}{12} & \frac{13}{12} & \frac{1}{4} \\ \frac{1}{12} & -\frac{1}{4} & -\frac{3}{4} & \frac{11}{12} \\ -\frac{1}{4} & \frac{5}{4} & -\frac{7}{4} & \frac{3}{4} \\ -\frac{1}{6} & \frac{1}{2} & -\frac{1}{2} & \frac{1}{6} \end{bmatrix}$$

$$\mathbf{R}_2 = \begin{bmatrix} -\frac{1}{12} & \frac{7}{12} & \frac{7}{12} & -\frac{1}{12} \\ \frac{1}{12} & -\frac{5}{4} & \frac{5}{4} & -\frac{1}{12} \\ \frac{1}{4} & -\frac{1}{4} & -\frac{1}{4} & \frac{1}{4} \\ -\frac{1}{6} & \frac{1}{2} & -\frac{1}{2} & \frac{1}{6} \end{bmatrix} \tag{A1.2}$$

$$\mathbf{R}_3 = \begin{bmatrix} \frac{1}{4} & \frac{13}{12} & -\frac{5}{12} & \frac{1}{12} \\ -\frac{11}{12} & \frac{3}{4} & \frac{1}{4} & -\frac{1}{12} \\ \frac{3}{4} & -\frac{7}{4} & \frac{5}{4} & -\frac{1}{4} \\ -\frac{1}{6} & \frac{1}{2} & -\frac{1}{2} & \frac{1}{6} \end{bmatrix}$$

$$\mathbf{R}_4 = \begin{bmatrix} \frac{25}{12} & -\frac{23}{12} & \frac{13}{12} & -\frac{1}{4} \\ -\frac{35}{12} & \frac{23}{4} & -\frac{15}{4} & \frac{11}{12} \\ \frac{5}{4} & -\frac{13}{4} & \frac{11}{4} & -\frac{3}{4} \\ -\frac{1}{6} & \frac{1}{2} & -\frac{1}{2} & \frac{1}{6} \end{bmatrix}$$

8 Appendix B

Given the third order polynomial

$$\rho_j(x) = (\rho_{i+1/2})_j + \sum_{k=1}^{3} a_{k,j} x^k \tag{A2.1}$$

the smoothness indicators are defined as

$$IS_{j,L} = \sum_{k=1}^{3} \int_{x_i - \Delta x/2}^{x_i + \Delta x/2} \Delta x^{2k-1} \left(\frac{d^k \rho_j}{dx^k} \right)^2 dx \qquad IS_{j,R} = \sum_{k=1}^{3} \int_{x_{i+1} - \Delta x/2}^{x_{i+1} + \Delta x/2} \Delta x^{2k-1} \left(\frac{d^k \rho_j}{dx^k} \right)^2 dx \tag{A2.2}$$

Since the reconstruction direction x is taken with respect to the face centre $\boldsymbol{x}_f$ and non-dimensionalized with $\Delta x = \left\| \boldsymbol{x}_\mathrm{P} - \boldsymbol{x}_\mathrm{N} \right\|$, the above expressions can be simplified and generalized as follows.

$$IS_{j,K} = r \sum_{k=1}^{3} \int_0^r \left(\frac{d^k \rho_j}{dx^k} \right)^2 dx \qquad \text{where} \quad r = \begin{cases} -1, & \text{if } K = L \\ +1, & \text{f } K = R \end{cases} \tag{A2.3}$$

Substituting Eq. (A2.1) into Eq. (A2.3), the expression in Eq. (13) can be obtained as follows.

$$\begin{aligned} IS_{j,K} &= r \left[\int_0^r \left(a_{0,j} + 2a_{1,j} x + 3a_{2,j} x^2 \right)^2 dx + \int_0^r \left(2a_{1,j} + 6a_{2,j} x \right)^2 dx + \int_0^r \left(6a_{2,j} \right)^2 dx \right] \\ &= r \left\{ \begin{array}{l} \left[a_{0,j}^2 x + 2a_{0,j} a_{1,j} x^2 + 2a_{0,j} a_{2,j} x^3 + \frac{4}{3} a_{1,j}^2 x^3 + 3a_{1,j} a_{2,j} x^4 + \frac{9}{5} a_{2,j}^2 x^5 \right]_0^r \\ + \left[4a_{1,j}^2 x + 12 a_{1,j} a_{2,j} x^2 + 12 a_{2,j}^2 x^3 \right]_0^r + \left[36 a_{2,j}^2 x \right]_0^r \end{array} \right\} \\ &= a_{0,j}^2 + 2r a_{0,j} a_{1,j} + 2a_{0,j} a_{2,j} + \tfrac{16}{3} a_{1,j}^2 + 15 r a_{1,j} a_{2,j} + \tfrac{249}{5} a_{2,j}^2 \\ &= \left(a_{0,j} + r a_{1,j} + a_{2,j} \right)^2 + \tfrac{13}{3} \left(a_{1,j} + \tfrac{3}{2} r a_{2,j} \right)^2 + \tfrac{781}{20} a_{2,j}^2 \end{aligned} \tag{A2.4}$$

Note that in the third and fourth lines of the above derivation, the following identity was used to simplify the result.

$$r^n = \begin{cases} 1, & \text{if } n \text{ is even} \\ r, & \text{if } n \text{ is odd} \end{cases}$$

9 References

[1] A. Harten. High resolution schemes for hyperbolic conservation laws. *J. Comput. Phys.*, 49:357-393, 1983

[2] E. Johnsen, J. Larsson, A.V. Bhagatwala, W.H. Cabot, P. Moin, B.J. Olson, P.S. Rawat, S.K. Shankar, B. Sjögreen, H.C. Yee, X. Zhong, and S.K. Lele. Assessment of high-resolution methods for numerical simulations of compressible turbulence with shock waves. *J. Comput. Phys.*, 229:1213-1237, 2010

[3] J.A. Ekaterinaris. High-order accurate, low numerical diffusion methods for aerodynamics. *Progress in Aerospace Sciences*. 41:192-300, 2005

[4] A. Harten, B. Engquist, S. Osher, and S.R. Chakravarthy. Uniformly high order accurate essentially non-oscillatory schemes, III. *J. Comput. Phys.*, 71:231-303, 1987

[5] X.-D. Liu, S. Osher, and T. Chan. Weighted essentially non-oscillatory schemes. *J. Comput. Phys.*, 115:200-212, 1994

[6] G.S. Jiang and C.W. Shu. Efficient implementation of weighted ENO schemes. *J. Comput. Phys.*, 126:202-228, 1996

[7] A.K. Henrick, T.D. Aslam, and J.M. Powers. Mapped weighted essentially non-oscillatory schemes: Achieving optimal order near critical points. *J. Comput. Phys.*, 207:542-567, 2005

[8] Y. Shen and G. Zha, Improved seventh-order WENO scheme, *48th AIAA Aerospace Sciences Meeting Including the New Horizons Forum and Aerospace Exposition*. 2010, American Institute of Aeronautics and Astronautics.

[9] M. Castro, B. Costa, and W.S. Don. High order weighted essentially non-oscillatory WENO-Z schemes for hyperbolic conservation laws. *J. Comput. Phys.*, 230:1766-1792, 2011

[10] H. Feng, F. Hu, and R. Wang. A new mapped weighted essentially non-oscillatory scheme. *J. Sci. Comput.*, 51:449-473, 2012

[11] H. Feng, C. Huang, and R. Wang. An improved mapped weighted essentially non-oscillatory scheme. *Appl. Math. Comput.*, 232:453-468, 2014

[12] F. Acker, R. B. de R. Borges, and B. Costa. An improved WENO-Z scheme. *J. Comput. Phys.*, 313:726-753, 2016

[13] R. Wang, H. Feng, and C. Huang. A new mapped weighted essentially non-oscillatory method using rational mapping function. *J. Sci. Comput.*, 67:540-580, 2016

[14] S.K. Godunov. A finite difference method for the computation of discontinuous solutions of the equations of fluid dynamics. *SB MATH+*. 47:357-393, 1959

[15] B. van Leer. Towards the ultimate conservative difference scheme. V. A second-order sequel to Godunov's method. *J. Comput. Phys.*, 32:101-136, 1979

[16] E.F. Toro, *Riemann solvers and numerical methods for fluid dynamics: a practical introduction*. 2013: Springer Science & Business Media.

[17] J. Qiu and C.W. Shu. On the construction, comparison, and local characteristic decomposition for high-order central WENO schemes. *J. Comput. Phys.*, 183:187-209, 2002

[18] N.A. Adams and K. Shariff. A high-resolution hybrid compact-ENO scheme for shock-turbulence interaction problems. *J. Comput. Phys.*, 127:27-51, 1996

[19] S. Pirozzoli. Conservative hybrid compact-WENO schemes for shock-turbulence interaction. *J. Comput. Phys.*, 178:81-117, 2002

[20] Y.-X. Ren, M.e. Liu, and H. Zhang. A characteristic-wise hybrid compact-WENO scheme for solving hyperbolic conservation laws. *J. Comput. Phys.*, 192:365-386, 2003

[21] D. Kim and J.H. Kwon. A high-order accurate hybrid scheme using a central flux scheme and a WENO scheme for compressible flowfield analysis. *J. Comput. Phys.*, 210:554-583, 2005

[22] B. Costa and W.S. Don. High order hybrid central-WENO finite difference scheme for conservation laws. *J. Comput. Appl. Math.*, 204:209-218, 2007

[23] X.Y. Hu, B. Wang, and N.A. Adams. An efficient low-dissipation hybrid weighted essentially non-oscillatory scheme. *J. Comput. Phys.*, 301:415-424, 2015

[24] J. Peng, C. Zhai, G. Ni, H. Yong, and Y. Shen. An adaptive characteristic-wise reconstruction WENO-Z scheme for gas dynamic Euler equations. *Comput. & Fluids*. 2018

[25] Y. Lee, W. Yao, and X. Fan, A low-dissipation scheme based on OpenFoam designed for large eddy simulation in compressible flow, *21st AIAA International Space Planes and Hypersonics Technologies Conference*. 2017, American Institute of Aeronautics and Astronautics.

[26] A. Bhagatwala and S.K. Lele. A modified artificial viscosity approach for compressible turbulence simulations. *J. Comput. Phys.*, 228:4965-4969, 2009

[27] F. Ducros, V. Ferrand, F. Nicoud, C. Weber, D. Darracq, C. Gacherieu, and T. Poinsot. Large-eddy simulation of the shock/turbulence interaction. *J. Comput. Phys.*, 152:517-549, 1999

[28] S. Gottlieb and C.W. Shu. Total variation diminishing Runge-Kutta schemes. *Math. Comp.*, 67:73-85, 1998

[29] D. Levy, G. Puppo, and G. Russo. Compact central WENO schemes for multidimensional conservation laws. *SIAM J. Sci. Comput.*, 22:656-672, 2000

[30] V.A. Titarev and E.F. Toro. Finite-volume WENO schemes for three-dimensional conservation laws. *J. Comput. Phys.*, 201:238-260, 2004

[31] K. Ritos, I.W. Kokkinakis, and D. Drikakis. Physical insight into the accuracy of finely-resolved iLES in turbulent boundary layers. *Comput. Fluids*. 169:309-316, 2018

[32] K. Ritos, I.W. Kokkinakis, and D. Drikakis. Performance of high-order implicit large eddy simulations. *Comput. Fluids*. 173:307-312, 2018

[33] A. Harten, P.D. Lax, and B. van Leer, On upstream differencing and Godunov-type schemes for hyperbolic conservation laws, *Upwind and High-Resolution Schemes*, M.Y. Hussaini, B. van Leer, and J. Van Rosendale, Editors. 1997, Springer Berlin Heidelberg: Berlin, Heidelberg. p. 53-79.

[34] E.F. Toro, M. Spruce, and W. Speares. Restoration of the contact surface in the HLL-Riemann solver. *Shock Waves*. 4:25-34, 1994

[35] G.A. Sod. A survey of several finite difference methods for systems of nonlinear hyperbolic conservation laws. *J. Comput. Phys.*, 27:1-31, 1978

[36] C.-W. Shu and S. Osher, Efficient implementation of essentially non-oscillatory shock-capturing schemes, II, *Upwind and High-Resolution Schemes*. 1989, Springer. p. 328-374.

[37] P. Lax and X. Liu. Solution of Two-Dimensional Riemann Problems of Gas Dynamics by Positive Schemes. *SIAM J. Sci. Comput.*, 19:319-340, 1998

[38] S. Karni. Multicomponent flow calculations by a consistent primitive algorithm. *J. Comput. Phys.*, 112:31-43, 1994

[39] E. Johnsen and T. Colonius. Implementation of WENO schemes in compressible multicomponent flow problems. *J. Comput. Phys.*, 219:715-732, 2006

[40] M. Pandolfi and D. D'Ambrosio. Numerical instabilities in upwind methods: analysis and cures for the “carbuncle” phenomenon. *J. Comput. Phys.*, 166:271-301, 2001

[41] J.J. Quirk, A contribution to the great Riemann solver debate, *Upwind and High-Resolution Schemes*, M.Y. Hussaini, B. van Leer, and J. Van Rosendale, Editors. 1997, Springer Berlin Heidelberg: Berlin, Heidelberg. p. 550-569.

[42] A.F. Emery. An evaluation of several differencing methods for inviscid fluid flow problems. *J. Comput. Phys.*, 2:306-331, 1968

[43] P. Woodward and P. Colella. The numerical simulation of two-dimensional fluid flow with strong shocks. *J. Comput. Phys.*, 54:115-173, 1984

[44] H.C. Yee, N.D. Sandham, and M.J. Djomehri. Low-dissipative high-order shock-capturing methods using characteristic-based filters. *J. Comput. Phys.*, 150:199-238, 1999

[45] U S Vevek, B. Zang, and T.H. New. On alternative setups of the double Mach reflection problem. *J. Sci. Comput.*, 78:1291-1303, 2019